

hp-adaptive discontinuous Galerkin methods for simplified P_N approximations of frequency-dependent radiative transfer

Stefano Giani*

Mohammed Seaid†

Abstract

We investigate the performance of a class of *hp*-adaptive discontinuous Galerkin methods for the numerical solution of simplified P_N approximations of radiative transfer in non-grey semitransparent media. By introducing an optical scale and using asymptotic expansions in the radiative transfer equation we formulate the simplified P_N approximations. The optical spectrum is decomposed in frequency bands and the simplified P_N equations are solved for each frequency band. As a numerical solver for the simplified P_N equations we consider a high-order discontinuous Galerkin method. The solver belongs to a class of finite element methods whose approximate solutions are discontinuous across inter-element boundaries; this property renders the method ideally suited for the *hp*-adaptivity. An error estimator is shown to provide reliable and practically useful upper bounds for the numerical errors independent of the optical scales used in the simulations. The proposed method is simple, fast and highly accurate. The performance of the method is analyzed on several applications in frequency-dependent radiative transfer. The aim of such a method compared to the conventional finite element methods is to solve the simplified P_N equations efficiently and with a high level of accuracy on unstructured meshes with different elements. The obtained results demonstrate the ability of the proposed method to capture the main radiative features.

Keywords. Radiative transfer; Simplified P_N approximations; Discontinuous Galerkin method; *hp*-adaptivity; Non-grey media

1 Introduction

There is a vast literature dealing with numerical methods for the radiative transfer equations, see for example [22,27] for a survey. These equations have been the key to understand the thermal radiation distribution on many semitransparent materials. As a well established example, the temperature distribution during the cooling process of glass which has direct effect on the quality of the product. Moreover, numerical experiments on semitransparent materials have shown that the heat transfer can not be estimated only by conduction but also by radiation. For instance, in many annealing processes, the media temperature is higher than 1000 K and at this temperature radiative transfer dominates conduction. The main difficulties raised when solving numerically the radiative transfer equations lie essentially on the large set of depend unknowns, the coupling between the radiative transfer and the heat conduction, and the specular reflecting boundary conditions. The most accurate procedures available for computing radiative transfer in semitransparent materials are the zonal and Monte Carlo methods [22]. However, these methods are not widely applied in comprehensive radiative transfer calculations due to their large computational time and memory storage requirements. Also, the equation of radiative transfer is in a non-differential form, a significant inconvenience when solved in conjunction with the differential equations of conduction and convection. For this reason, numerous investigations are currently being carried out worldwide to assess

*School of Engineering and Computing Sciences, University of Durham, South Road, Durham DH1 3LE, UK *E-mail:* stefano.giani@durham.ac.uk

†School of Engineering and Computing Sciences, University of Durham, South Road, Durham DH1 3LE, UK *E-mail:* m.seaid@durham.ac.uk

computationally efficient methods in radiative transfer applications. The present work deals with the design of such methods.

In the current study, we consider the simplified P_N (SP_N) approximations to the radiative transfer equations. The SP_N approximations were first proposed in [14] and theoretically studied in [19]. In [20, 26], the SP_N approximations have been extensively studied for radiative transfer in glass manufacturing, while in [13] they have been implemented for radiation in gas turbines. The SP_N approximations have also been studied in [6] for internal radiation in crystal growth. The main advantage in considering SP_N approximations is the fact that the radiative transfer equations are transformed to a mixed set of elliptic equations independent of the angular directions and easy to solve numerically. Furthermore, comparisons presented in the previous references proved that in optically thick media (large absorption) the SP_N models approximate the full radiative transfer equation with less computational cost and give results which are more accurate than those obtained by the classical Rosseland approach traditionally used by physicists. The physical phenomena in many radiative applications can be modeled by the SP_N equations with the property that the media is optically thick, particularly when certain nondimensional parameters reach small values. As example of these parameters, we mention the optical scale. It is well established that for small values of this parameter, the SP_N approximations are sources of computational difficulties and nonphysical oscillations. On the other hand, steep fronts and boundary layers are among the difficulties that most numerical methods fail to resolve accurately. Indeed, such practical radiative problems are not trivial to simulate because the geometry can be complex and internal source terms may produce steep gradients in the vicinity of the boundary along the computational domain. It is well known that unstructured grids can be highly advantageous on the basis of their ability to provide local mesh refinement near important thermal features and structures. As a consequence, the ability to provide local mesh refinement where it is needed leads to improved accuracy for a given computational cost as compared with methods that use structured meshes. The conventional continuous finite element method has been applied in [18] to solve the SP_N approximations for a glass cooling process. The h -adaptivity has also been implemented in this reference to resolve boundary layers for this class of problems. However, for practical applications, this method may become computationally demanding due to the lack of *a posteriori* error analysis.

As for most mesh-based methods for solving partial differential equations (PDEs), the computational cost in finite element methods becomes more and more important (sometimes prohibitive) when we need numerical solution with high accuracy. It is also well known that *a posteriori* error analysis is one approach to find a compromise between cost and accuracy in these methods. The development of Discontinuous Galerkin (DG) methods for the numerical approximation of PDEs is an extremely exciting research topic, see [5, 7–10, 12, 15] among others. The DG methods have several important advantages over the well established finite volume and finite element methods. The concept of high order discretization is inherent to the DG method. Moreover, due to the simple communication at element interfaces, elements with so-called hanging nodes can be easily treated. Additionally, the communication at element interfaces is identical for any order of the method, which simplifies the use of methods with different polynomial orders p in adjacent elements. The flexibility of DG methods makes them ideal for hp -adaptivity, which is a technique where both the size of the elements (h -adaptivity) and their polynomial orders (p -adaptivity) are adjusted to improve the accuracy of the solution. In the current study we derive *a posteriori* error estimates for the DG discretization of SP_N approximations in frequency-dependent radiative transfer applications. The natural combination of adaptive techniques with DG method retains the best features of both methods and overcomes many of their defects. Their implementation relies on the projection operators, whose actions use only standard nodal data structures and can be evaluated locally at the element level. In order to be even more efficient, in this paper we use anisotropic h -adaptivity which has been proved to work very well in presence of boundary layers generating long and thin elements along them. The gain in efficiency using adaptivity is directly related to the accuracy of the error estimator which is used to estimate the distribution of the solution error on the mesh to guide the adaptive procedure. The error estimator used in this work is a modification of the error estimator in [15] to solve the SP_N problems. We numerically illustrate the efficiency of our techniques by solving several test examples for radiative transfer problems in both grey and non-grey media. The method is also used to solve a radiative transfer problem with discontinuous

coefficients. Solving the SP_N approximations using a DG method with hp -adaptivity, to the best of our knowledge, is reported for the first time.

The present paper is organized as follows. Description of the simplified P_N approximations of radiative transfer in non-grey semitransparent media is presented in section 2. Section 3 is devoted to the formulation of hp -adaptive discontinuous Galerkin methods. This section includes the discontinuous Galerkin discretization and the hp -error estimations for the simplified P_N equations. In section 4, we present numerical results and examples for the simplified P_N approximations of frequency-dependent radiative transfer. Our new approach is shown to enjoy the expected accuracy as well as the efficiency. Concluding remarks are given in section 5.

2 Simplified P_N approximations of radiative transfer

Let Ω be a geometrical domain with a boundary $\partial\Omega$ of an absorbing and emitting semitransparent material with a given steady temperature distribution T in Ω and T_b on the boundary $\partial\Omega$. The spectral intensity $I(\mathbf{x}, \mathbf{s}, \nu)$ at the space point \mathbf{x} , within the frequency ν and along the direction \mathbf{s} , is obtained from the dimensionless radiative transfer equation

$$\epsilon \mathbf{s} \cdot \nabla I + (\kappa + \sigma) I = \frac{\sigma}{4\pi} \int_{S^2} I(\mathbf{x}, \mathbf{s}', \nu) ds' + \kappa B(T, \nu, n_m), \quad (\mathbf{x}, \mathbf{s}, \nu) \in \Omega \times S^2 \times]\nu_0, \infty), \quad (2.1)$$

where ϵ is the optical thickness coefficient, $\kappa(\nu)$ the absorption coefficient, $\sigma(\nu)$ the scattering coefficient and $B(T, \nu, n)$ is the spectral intensity of the black-body radiation given by the Planck function in a medium with refractive index n as

$$B(T, \nu, n) = \frac{2h_P\nu^3}{c_0^2} n^2 (e^{h_P\nu/k_B T} - 1)^{-1}, \quad (2.2)$$

where h_P , k_B and c_0 are Planck constant, Boltzmann constant and the speed of radiation propagation in the vacuum, respectively [21]. Note that the equation (2.1) models the changes of an intensity $I(\mathbf{x}, \mathbf{s}, \nu)$ as particles are passing through the domain Ω at the position point \mathbf{x} along the direction \mathbf{s} in the unit sphere S^2 with the frequency ν and are subject to losses due to absorption κ and scattering σ , while their number grows due to the black-body radiation source $B(T, \nu, n_m)$ inside a semitransparent media with the refractive index n_m . On the boundary we consider transmitting and specular reflecting conditions

$$I(\hat{\mathbf{x}}, \mathbf{s}, \nu) - \rho(\mathbf{n} \cdot \mathbf{s}) I(\hat{\mathbf{x}}, \mathbf{s}', \nu) = (1 - \rho(\mathbf{n} \cdot \mathbf{s})) B(T_b, \nu, n_b), \quad (\hat{\mathbf{x}}, \mathbf{s}, \nu) \in \partial\Omega^- \times S^2 \times]\nu_0, \infty), \quad (2.3)$$

where $\partial\Omega^-$ is the boundary region defined as

$$\partial\Omega^- = \left\{ \hat{\mathbf{x}} \in \partial\Omega; \quad \mathbf{n}(\hat{\mathbf{x}}) \cdot \mathbf{s} < 0 \right\},$$

with $\mathbf{n}(\hat{\mathbf{x}})$ denotes the outward normal in $\hat{\mathbf{x}}$ with respect to $\partial\Omega$. In (2.3), $\mathbf{s}' = \mathbf{s} - 2(\mathbf{n} \cdot \mathbf{s})\mathbf{n}$ is the specular reflection of \mathbf{s} on $\partial\Omega$, and $\rho \in [0, 1]$ is the reflectivity obtained according to the Fresnel and Snell laws [27]. Thus, for an incident angle θ_m given by $\cos \theta_m = |\mathbf{n} \cdot \mathbf{s}|$ and Snell's law

$$n_b \sin \theta_b = n_m \sin \theta_m,$$

the reflectivity $\rho(\mu)$, $\mu = |\mathbf{n} \cdot \mathbf{s}|$, is defined as follows

$$\rho(\mu) = \begin{cases} \frac{1}{2} \left(\frac{\tan^2(\theta_m - \theta_b)}{\tan^2(\theta_m + \theta_b)} + \frac{\sin^2(\theta_m - \theta_b)}{\sin^2(\theta_m + \theta_b)} \right), & \text{if } |\sin \theta_m| \leq \frac{n_b}{n_m}, \\ 1, & \text{otherwise,} \end{cases} \quad (2.4)$$

where n_b and n_m are the refractive indices of the surrounding medium and the semitransparent material, respectively.

In the current study we assume that the spectral absorption $\kappa(\nu)$ and the scattering $\sigma(\nu)$ are piecewise constants with respect to the frequency ν , *i.e.*

$$\kappa(\nu) = \kappa_k, \quad \sigma(\nu) = \sigma_k, \quad \forall \nu \in [\nu_{k-1}, \nu_k), \quad k = 1, 2, \dots, N_\nu, \quad (2.5)$$

with κ_k and σ_k are constants and N_ν is the total number of spectral bands. If we denote the intensity of the k th spectral band by

$$I^{(k)}(\mathbf{x}, \mathbf{s}) = \int_{\nu_k}^{\nu_{k+1}} I(\mathbf{x}, \mathbf{s}, \nu) d\nu,$$

then the radiative transfer equations (2.1) and (2.3) can be rewritten as

$$\begin{aligned} \varepsilon \mathbf{s} \cdot \nabla I^{(k)} + (\kappa_k + \sigma_k) I^{(k)} &= \frac{\sigma_k}{4\pi} \varphi^{(k)} + \kappa_k B^{(k)}(T, n_m), \\ I^{(k)}(\hat{\mathbf{x}}, \mathbf{s}) - \rho(\mathbf{n} \cdot \mathbf{s}) I^{(k)}(\hat{\mathbf{x}}, \mathbf{s}') &= \left(1 - \rho(\mathbf{n} \cdot \mathbf{s})\right) B^{(k)}(T_b, n_b), \end{aligned} \quad (2.6)$$

where the mean intensity $\varphi^{(k)}$ and the Planckian function $B^{(k)}$ are given by

$$\varphi^{(k)}(\mathbf{x}) = \int_{S^2} I^{(k)}(\mathbf{x}, \mathbf{s}) d\mathbf{s} \quad \text{and} \quad B^{(k)}(T, n) = \int_{\nu_k}^{\nu_{k+1}} B(T, \nu, n) d\nu,$$

respectively. Note that many physical assumptions have to be taken into account to derive well-posed models for radiative transfer equations in non-grey diffusive semitransparent media. For more details on these assumptions, we refer to [22, 27] among others. In what follows, we briefly recast the SP_N approximations for the radiative transfer equations (2.6). For more analysis we refer the reader to [20] and further references can be found therein. Hence, we write the first equation in (2.6) as

$$\left(1 + \frac{\varepsilon}{\kappa_k + \sigma_k} \mathbf{s} \cdot \nabla\right) I^{(k)} = Q^{(k)},$$

where the source term

$$Q^{(k)} = \frac{\sigma_k}{4\pi(\kappa_k + \sigma_k)} \varphi^{(k)} + \frac{\kappa_k}{\kappa_k + \sigma_k} B^{(k)}(T, n_m).$$

We then apply a Neumann series to formally invert the transport operator as

$$\begin{aligned} I^{(k)} &= \left(1 + \frac{\varepsilon}{\kappa_k + \sigma_k} \mathbf{s} \cdot \nabla\right)^{-1} Q^{(k)}, \\ &\approx \left(1 - \frac{\varepsilon}{\kappa_k + \sigma_k} \mathbf{s} \cdot \nabla + \frac{\varepsilon^2}{(\kappa_k + \sigma_k)^2} (\mathbf{s} \cdot \nabla)^2 - \frac{\varepsilon^3}{(\kappa_k + \sigma_k)^3} (\mathbf{s} \cdot \nabla)^3 + \frac{\varepsilon^4}{(\kappa_k + \sigma_k)^4} (\mathbf{s} \cdot \nabla)^4 \dots\right) Q^{(k)}. \end{aligned}$$

Integrating with respect to \mathbf{s} over all directions in the unit sphere and using the relation

$$\int_{S^2} (\mathbf{s} \cdot \nabla)^n d\mathbf{s} = \left(1 + (-1)^n\right) \frac{2\pi}{n+1} \nabla^n,$$

we obtain the formal asymptotic equation for $\varphi^{(k)}$

$$4\pi Q^{(k)} = \left(1 - \frac{\varepsilon^2}{3(\kappa_k + \sigma_k)^2} \nabla^2 - \frac{4\varepsilon^4}{45(\kappa_k + \sigma_k)^4} \nabla^4 - \frac{44\varepsilon^6}{94(\kappa_k + \sigma_k)^6} \nabla^6\right) \varphi^{(k)} + \mathcal{O}(\varepsilon^8).$$

When terms of order $\mathcal{O}(\varepsilon^2)$, $\mathcal{O}(\varepsilon^4)$, $\mathcal{O}(\varepsilon^6)$ or $\mathcal{O}(\varepsilon^8)$ are neglected we obtain the SP_0 , SP_1 , SP_2 or SP_3 approximations, respectively. Higher order approximations can also be derived similarly. In this paper, we consider only the SP_1 and SP_3 approximations, and our DG method can straightforwardly be extended to other approximations. The boundary conditions for SP_N approximations are obtained from variational

principles and are connected to the Marshak conditions for P_N approximations, compare [22]. Here, we briefly state the set of equations for each SP_N approximation and for more details we refer to [20].

For the SP_1 approximation:

$$4\pi Q^{(k)} = \varphi^{(k)} - \frac{\varepsilon^2}{3(\kappa_k + \sigma_k)^2} \nabla^2 \varphi^{(k)} + \mathcal{O}(\varepsilon^4),$$

and the SP_1 model reads

$$\begin{aligned} -\nabla \cdot \left(\frac{\varepsilon^2}{3(\kappa_k + \sigma_k)} \nabla \varphi^{(k)} \right) + \kappa_k \varphi^{(k)} &= 4\pi \kappa_k B^{(k)}(T, n_m), \\ \varphi^{(k)} + \left(\frac{1 + 3r_2}{1 - 2r_1} \frac{2\varepsilon}{3(\kappa_k + \sigma_k)} \right) \mathbf{n}(\hat{\mathbf{x}}) \cdot \nabla \varphi^{(k)} &= 4\pi B^{(k)}(T_b, n_b). \end{aligned} \quad (2.7)$$

The variables r_1 and r_2 appeared in the boundary conditions for $\varphi^{(k)}$ depend on reflectivity of the considered media and are given in appendix A.

For the SP_3 approximation:

$$\begin{aligned} 4\pi Q^{(k)} &= \left(1 - \frac{\varepsilon^2}{3(\kappa_k + \sigma_k)^2} \nabla^2 - \frac{4\varepsilon^4}{45(\kappa_k + \sigma_k)^4} \nabla^4 - \frac{44\varepsilon^6}{945(\kappa_k + \sigma_k)^6} \nabla^6 \right) \varphi^{(k)} + \mathcal{O}(\varepsilon^8), \\ &= \varphi^{(k)} - \frac{\varepsilon^2}{3(\kappa_k + \sigma_k)^2} \nabla^2 \left(\varphi^{(k)} + \left(1 + \frac{11\varepsilon^2}{21(\kappa_k + \sigma_k)^2} \nabla^2 \right) \left(\frac{4\varepsilon^2}{15(\kappa_k + \sigma_k)^2} \varphi^{(k)} \right) \right) + \mathcal{O}(\varepsilon^8), \\ &= \varphi^{(k)} - \frac{\varepsilon^2}{3(\kappa_k + \sigma_k)^2} \nabla^2 \left(\varphi^{(k)} + \left(1 - \frac{11\varepsilon^2}{21(\kappa_k + \sigma_k)^2} \nabla^2 \right)^{-1} \left(\frac{4\varepsilon^2}{15(\kappa_k + \sigma_k)^2} \varphi^{(k)} \right) \right) + \mathcal{O}(\varepsilon^8), \end{aligned}$$

which can be reformulated up to $\mathcal{O}(\varepsilon^8)$ as

$$4\pi Q^{(k)} = \varphi^{(k)} - \frac{\varepsilon^2}{3(\kappa_k + \sigma_k)^2} \nabla^2 \left(\varphi^{(k)} + 2\varphi_2^{(k)} \right)$$

or

$$-\frac{\varepsilon^2}{3(\kappa_k + \sigma_k)^2} \nabla^2 \left(\varphi^{(k)} + 2\varphi_2^{(k)} \right) + \kappa_k \varphi^{(k)} = 4\pi \kappa_k Q^{(k)},$$

where

$$\varphi_2^{(k)} = \left(1 - \frac{11\varepsilon^2}{21(\kappa_k + \sigma_k)^2} \nabla^2 \right)^{-1} \left(\frac{2\varepsilon^2}{15(\kappa_k + \sigma_k)^2} \varphi^{(k)} \right).$$

Expanding this equations yields

$$\begin{aligned} \frac{11\varepsilon^2}{21(\kappa_k + \sigma_k)^2} \nabla^2 \varphi_2^{(k)} + \varphi_2^{(k)} &= \frac{2\varepsilon^2}{15(\kappa_k + \sigma_k)^2} \varphi^{(k)} \nabla^2 \varphi^{(k)}, \\ &= \frac{2}{5} \left(-4\pi Q^{(k)} + \varphi^{(k)} - \frac{2\varepsilon^2}{3(\kappa_k + \sigma_k)^2} \nabla^2 \varphi_2^{(k)} \right), \end{aligned}$$

or simply

$$\nabla \cdot \left(\frac{9\varepsilon^2}{35(\kappa_k + \sigma_k)} \nabla \psi_1^{(k)} \right) \varphi_2^{(k)} + \frac{2}{5} \kappa_k \varphi_2^{(k)} - \frac{2}{5} \kappa_k \varphi^{(k)} = \frac{8}{5} \pi \kappa_k B^{(k)}(\Theta, n_m).$$

For computational reasons, by introducing the variables $\psi_1^{(k)}$ and $\psi_2^{(k)}$ such as

$$\varphi^{(k)} = \frac{\gamma_2 \psi_1^{(k)} - \gamma_1 \psi_2^{(k)}}{\gamma_2 - \gamma_1}, \quad \text{and} \quad \varphi_2^{(k)} = \frac{\psi_2^{(k)} - \psi_1^{(k)}}{\gamma_2 - \gamma_1},$$

the SP₃ model is defined as

$$\begin{aligned}
-\nabla \cdot \left(\frac{\varepsilon^2 \mu_1^2}{\kappa_k + \sigma_k} \nabla \psi_1^{(k)} \right) + \kappa_k \psi_1^{(k)} &= 4\pi \kappa_k B^{(k)}(\Theta, n_m), \\
-\nabla \cdot \left(\frac{\varepsilon^2 \mu_2^2}{\kappa_k + \sigma_k} \nabla \psi_2^{(k)} \right) + \kappa_k \psi_2^{(k)} &= 4\pi \kappa_k B^{(k)}(\Theta, n_m), \\
\alpha_1 \psi_1 + \frac{\varepsilon}{\kappa_k + \sigma_k} \mathbf{n}(\hat{\mathbf{x}}) \cdot \nabla \psi_1^{(k)} &= -\beta_2 \psi_2^{(k)} + \eta_1 B^{(k)}(\Theta_b, n_b), \\
\alpha_2 \psi_2 + \frac{\varepsilon}{\kappa_k + \sigma_k} \mathbf{n}(\hat{\mathbf{x}}) \cdot \nabla \psi_2^{(k)} &= -\beta_1 \psi_1^{(k)} + \eta_2 B^{(k)}(\Theta_b, n_b).
\end{aligned} \tag{2.8}$$

A detailed discussion on the formulation of equations (2.8) can be found in [20]. The mean radiative intensity $\varphi^{(k)}$ is obtained from the variables $\psi_1^{(k)}$ and $\psi_2^{(k)}$ according to the relation

$$\varphi^{(k)} = \frac{\gamma_2 \psi_1^{(k)} - \gamma_1 \psi_2^{(k)}}{\gamma_2 - \gamma_1}, \quad k = 1, 2, \dots, N_\nu.$$

The parameters μ_i , α_i , β_i , η_i , and γ_i ($i = 1, 2$) are derived using asymptotic and variational analyses, see reference [20]. For completeness, the corresponding formulas for calculating these parameters are listed in appendix A.

3 hp-adaptive discontinuous Galerkin methods

In this section we formulate our DG method for solving the SP₁ and SP₃ approximations given by the systems (2.7) and (2.8), respectively. We also describe the error estimators used for the *hp*-adaptivity procedures. For simplicity in the presentation, the SP_N approximations can be rearranged in a compact form as

$$\begin{aligned}
-\nabla \cdot (A \nabla \phi) + B \phi &= F, \\
C \mathbf{n}(\hat{\mathbf{x}}) \cdot \nabla \phi + D \phi &= G,
\end{aligned} \tag{3.1}$$

where the variables in the compact form (3.1) are defined as

$$\begin{aligned}
\phi = \varphi, \quad A = \frac{\varepsilon^2}{3(\kappa_k + \sigma_k)}, \quad B = \kappa_k, \quad C = \frac{1 + 3r_2}{1 - 2r_1} \frac{2\varepsilon}{3(\kappa_k + \sigma_k)}, \quad D = 1, \\
F = 4\pi \kappa_k B^{(k)}(T, n_m), \quad G = 4\pi B^{(k)}(T_b, n_b),
\end{aligned}$$

for the SP₁ approximation, and

$$\begin{aligned}
\phi = \begin{pmatrix} \psi_1 \\ \psi_2 \end{pmatrix}, \quad A = \begin{pmatrix} \frac{\varepsilon^2 \mu_1^2}{\kappa_k + \sigma_k} & 0 \\ 0 & \frac{\varepsilon^2 \mu_2^2}{\kappa_k + \sigma_k} \end{pmatrix}, \quad B = \begin{pmatrix} \kappa_k \\ \kappa_k \end{pmatrix}, \quad C = \begin{pmatrix} \frac{\varepsilon}{\kappa_k + \sigma_k} \\ \frac{\varepsilon}{\kappa_k + \sigma_k} \end{pmatrix}, \\
D = \begin{pmatrix} \alpha_1 & \beta_2 \\ \beta_1 & \alpha_2 \end{pmatrix}, \quad F = \begin{pmatrix} 4\pi \kappa_k B^{(k)}(T, n_m) \\ 4\pi \kappa_k B^{(k)}(T, n_m) \end{pmatrix}, \quad G = \begin{pmatrix} \eta_1 B^{(k)}(T_b, n_b) \\ \eta_2 B^{(k)}(T_b, n_b) \end{pmatrix},
\end{aligned}$$

for the SP₃ approximation. It should be pointed out that all the numerical methods presented in the literature for the SP₃ system, decouple the equations (2.8) by solving the equations for ψ_1 and ψ_2 separately using an iterative procedure on the boundary. Here the SP₃ approximation is solved in a fully coupled manner and no iterations are needed for the boundary conditions.

To formulate our DG method, we first require a discretization of the space domain $\Omega \cup \partial\Omega$. To perform this step, we generate a mesh $\mathcal{T} = \{K\}$ to be a shape-regular subdivision of Ω , with K denoting a generic element. We assume everywhere in the paper, with the only exception of Section 4.4, that the subdivision \mathcal{T} is constructed via affine mappings $F_K : \hat{K} \rightarrow K$ with non-singular Jacobian where \hat{K} is the reference square or triangle, depending on the type of element. In Section 4.4 we use the transfinite interpolation method [25] to handle curved geometries. The generated mesh is allowed to contain at most one hanging node per edge. We also use the notation $\mathcal{E}(\mathcal{T})$ and $\mathcal{E}^{int}(\mathcal{T}) \subset \mathcal{E}(\mathcal{T})$ to denote the set of all edges in the triangulation \mathcal{T} and the subset of all interior edges and by $\mathcal{E}^{BC}(\mathcal{T}) \subset \mathcal{E}(\mathcal{T})$ the subset of all boundary edges, respectively. In case of quadrilateral elements, we define the following quantities for anisotropic meshes. For each quadrilateral element $K \in \mathcal{T}$, we define the two anisotropic vectors \underline{v}_K^1 and \underline{v}_K^2 . These vectors reflect the two anisotropic directions of the generic element K and their lengths are denoted by h_K^1 and h_K^2 , respectively. Thus,

$$h_K^1 = \text{length}(\underline{v}_K^1), \quad h_K^2 = \text{length}(\underline{v}_K^2).$$

We also set

$$h_{\min,K} = \min(h_K^1, h_K^2), \quad h_{\max,K} = \max(h_K^1, h_K^2).$$

Let \mathbf{M}_K denote the matrix formed by the anisotropic vectors \underline{v}_K^1 and \underline{v}_K^2 as

$$\mathbf{M}_K = \begin{pmatrix} \underline{v}_K^1 & \underline{v}_K^2 \end{pmatrix}. \quad (3.2)$$

Note that the matrix \mathbf{M}_K is orthogonal and it satisfies

$$\mathbf{M}_K^\top \mathbf{M}_K = \begin{pmatrix} (h_K^1)^2 & 0 \\ 0 & (h_K^2)^2 \end{pmatrix}.$$

Given an edge $E \in \mathcal{E}(\mathcal{T})$, for any element $K \in \mathcal{T}$, if $E \in \mathcal{E}(K)$ or E is a part of an elemental edge of K , we define a local function of the edge E as

$$h_{E,K}^\perp = h_K^{3-i}, \quad \text{if } E \text{ is parallel to } \underline{v}_K^i, \quad i = 1, 2.$$

Moreover, for any $E \in \mathcal{E}^{int}(\mathcal{T})$, we assume that

$$h_{E,K}^\perp \sim h_{E,K'}^\perp, \quad E = K \cap K', \quad K, K' \in \mathcal{T}. \quad (3.3)$$

Notice that the assumption (3.3) does not bound the aspect ratios of elements. For any edges $E, E' \in \mathcal{E}(K)$ and $E \cap E' \neq \emptyset$, $h_E/h_{E'}$ can be significantly large. If $E \in \mathcal{E}(K)$ is parallel to \underline{v}_K^i , $i = 1, 2$, we define

$$h_{E,K} = h_K^i, \quad i = 1, 2.$$

For any edge $E \in \mathcal{E}(\mathcal{T})$, we further set

$$h_E^\perp = \begin{cases} \min(h_{E,K}^\perp, h_{E,K'}^\perp), & \text{if } E \in \mathcal{E}^{int}(\mathcal{T}), \quad E = \partial K \cap \partial K', \\ h_{E,K}^\perp, & \text{if } E \in \mathcal{E}(\mathcal{T}) \setminus \mathcal{E}^{int}(\mathcal{T}), \quad E = \partial K \cap \partial\Omega. \end{cases}$$

In our analysis, we allow for irregularly refined meshes \mathcal{T} , where each elemental edge $E \in \mathcal{E}(K)$ may contain one hanging node in the middle. We then define $h_{\min,E}$ by

$$h_{\min,E} = \begin{cases} \min(h_{\min,K}, h_{\min,K'}), & \text{if } E \in \mathcal{E}^{int}(\mathcal{T}), \quad E = \partial K \cap \partial K', \\ h_{\min,K}, & \text{if } E \in \mathcal{E}(\mathcal{T}) \setminus \mathcal{E}^{int}(\mathcal{T}), \quad E = \partial K \cap \partial\Omega, \end{cases}$$

It is evident that the assumption (3.3) implies that for any edge $E \in \mathcal{E}(\mathcal{T})$ and any element $K \in \mathcal{T}$, if $E \in \mathcal{E}(K)$ or E is a part of one element edge in K , one obtains

$$h_E^\perp \sim h_{E,K}^\perp, \quad h_{\min,E} \sim h_{\min,K}. \quad (3.4)$$

In case of triangular elements, all the quantities for anisotropic meshes are redefined with isotropic quantities re-defining the following quantities as:

$$h_K^1 = h_K^2 = h_K, \quad h_{E,K}^\perp = h_{E,K},$$

where h_K is the size of the element and $h_{E,K}$ is the size of the edge E of the element.

Next we introduce the polynomial degrees for the approximation in our DG method. Hence, for each element K of the mesh \mathcal{T} we associate a polynomial degree $p_K \geq 1$ and we introduce the degree vector $\mathbf{p} = \{p_K : K \in \mathcal{T}\}$, with $|\mathbf{p}| = \max_{K \in \mathcal{T}} p_K$. We assume that \mathbf{p} is of bounded local variation in the sense that for any pair of neighboring elements $K, K' \in \mathcal{T}$, we have

$$\varrho^{-1} \leq \frac{p_K}{p_{K'}} \leq \varrho, \quad (3.5)$$

where $\varrho \geq 1$ is a constant independent of the particular mesh in a sequence of meshes. For any $E \in \mathcal{E}(\mathcal{T})$, we introduce the edge polynomial degree p_E by

$$p_E = \begin{cases} \max(p_K, p_{K'}), & \text{if } E = \partial K \cap \partial K' \in \mathcal{E}^{int}(\mathcal{T}), \\ p_K, & \text{if } E = \partial K \cap \partial \Omega \in \mathcal{E}(\mathcal{T}) \setminus \mathcal{E}^{int}(\mathcal{T}). \end{cases} \quad (3.6)$$

Hence, for a given partition \mathcal{T} of Ω and a degree vector \mathbf{p} on \mathcal{T} , we define the hp -version DG finite element space by

$$V_{\mathbf{p}}(\mathcal{T}) = \left\{ v \in L^2(\Omega) : v|_K \in \mathcal{Q}_{p_K}(K), \quad K \in \mathcal{T} \right\},$$

with $\mathcal{Q}_{p_K}(K)$ denotes the set of all polynomials on the element K of degree less or equal to p_K .

Let \mathbf{n}_K denotes the outward unit normal on the boundary ∂K of an element K . Given an edge $E \in \mathcal{E}^{int}(\mathcal{T})$ shared by two elements K^+ and K^- , a vector field $\mathbf{v} \in H^{1/2}(\Omega) \times H^{1/2}(\Omega)$ and a scalar field $v \in H^{1/2}(\Omega)$, we define the jumps and the averages of \mathbf{v} and v across E by

$$\{v\} = \frac{1}{2} \left(v|_{\bar{K}^+} + v|_{\bar{K}^-} \right), \quad [v] = v|_{\bar{K}^+} \cdot \mathbf{n}_K + v|_{\bar{K}^-} \cdot \mathbf{n}_{K'}, \quad (3.7)$$

$$\{A\mathbf{v}\} = \frac{1}{2} \left(\omega^- \mathbf{v}|_{\bar{K}^+} + \omega^+ \mathbf{v}|_{\bar{K}^-} \right), \quad [A\mathbf{v}] = \omega^- \mathbf{v}|_{\bar{K}^+} \cdot \mathbf{n}_K + \omega^+ \mathbf{v}|_{\bar{K}^-} \cdot \mathbf{n}_{K'},$$

where $\omega^- = A^+ / (A^+ + A^-)$ and $\omega^+ = A^- / (A^+ + A^-)$, with A^+, A^- are the values of A on the edge from either elements. Note that if $E \subset \partial \Omega$, we set $\{\mathbf{v}\} = \mathbf{v}$, $[v] = v \cdot \mathbf{n}$, $\{v\} = v$ and $[v] = v\mathbf{n}$, with \mathbf{n} is the outward unit normal to the boundary $\partial \Omega$.

The derivation of the DG approximation for SP_1 and SP_3 equations can be performed using similar techniques as those reported in [5]. Thus, the DG approximation for the SP_1 problem reads as follows: Find $\phi_h \in V_{\mathbf{p}}(\mathcal{T})$ such that

$$B(\phi_h, v_h) + K_h(\phi_h, v_h) = (F, v_h) + \sum_{E \in \mathcal{E}^{BC}(\mathcal{T})} \int_E \frac{A}{C} G v_h ds, \quad \forall v_h \in V_{\mathbf{p}}(\mathcal{T}), \quad (3.8)$$

where the bilinear forms

$$B(w, v) = \sum_{K \in \mathcal{T}} \int_K (A \nabla w \cdot \nabla v + B w v) dx + \sum_{E \in \mathcal{E}^{int}(\mathcal{T})} \frac{2\gamma \omega^+ A^+ p_E^2}{h_E^\perp} \int_E [w] \cdot [v] ds, \quad (3.9)$$

$$K_h(w, v) = - \sum_{E \in \mathcal{E}^{int}(\mathcal{T})} \int_E \{A \nabla w\} \cdot [v] + \{A \nabla v\} \cdot [w] ds + \sum_{E \in \mathcal{E}^{BC}(\mathcal{T})} \int_E \frac{AD}{C} w v ds,$$

and (\cdot, \cdot) denotes the standard linear form. Similarly, the DG approximation for the SP₃ system reads as follows: Find $\phi_h \in V_{\mathbf{p}}(\mathcal{T}) \times V_{\mathbf{p}}(\mathcal{T})$ such that

$$B(\phi_h, v_h) + K_h(\phi_h, v_h) = (F, v_h) + \sum_{E \in \mathcal{E}^{BC}(\mathcal{T})} \int_E \frac{A}{C} G v_h ds, \quad \forall v_h \in V_{\mathbf{p}}(\mathcal{T}) \times V_{\mathbf{p}}(\mathcal{T}), \quad (3.10)$$

where B and K_h are defined in (3.9). Note that in general the penalty parameter in (3.9) $\gamma > 0$ is chosen large enough so that the operator $B + K_h$ is coercive.

In the presence of steep radiative gradients and boundary layers as those obtained by SP₁ and SP₃ approximations of radiative transfer, the above DG method would need an extremely refined meshes to resolve these radiative features. To overcome this difficulty in the present work we consider an anisotropic hp -adaptivity using a residual based *a posteriori* error estimate. Rigorous proofs for the error estimators in the SP₁ and SP₃ equations can be achieved using the same steps in [15] and therefore are omitted here. Hence, the error estimator for the considered problems is given by

$$\eta_{\text{err}} = \sqrt{\sum_{K \in \mathcal{T}} \left(\eta_{R,K}^2 + \eta_{B,K}^2 + \eta_{E,K}^2 + \eta_{J,K}^2 \right)}, \quad (3.11)$$

where the four terms under the sum are defined as

$$\begin{aligned} \eta_{R,K}^2 &= \alpha_K^2 \left\| F_h + \nabla \cdot (A \nabla \phi_h) - B \phi_h \right\|_{0,K}^2, \\ \eta_{B,K}^2 &= \sum_{E \in \mathcal{E}^{BC}(K)} A^{-1/2} \alpha_E \left\| A \nabla \phi_h \cdot \mathbf{n}_E + \frac{AD}{C} \phi_h - \frac{A}{C} G_h \right\|_{0,E}^2, \\ \eta_{E,K}^2 &= \sum_{E \in \mathcal{E}^{int}(K)} A_{\min}^{-1/2} \alpha_E \left\| [A \nabla \phi_h] \right\|_{0,E}^2, \\ \eta_{J,K}^2 &= \frac{1}{2} \sum_{E \in \mathcal{E}^{int}(K)} \left(\frac{\gamma^2 A_{\max} p_E^2}{h_{E,K}^\perp} + \frac{A_{\max} h_{E,K}^\perp p_E^2}{h_{\min,K}^2} + \frac{\kappa_{\min} h_{E,K}^\perp}{p_E^2} + \frac{A_{\max} p_E^2}{h_{E,K}^\perp} + \frac{A_{\max} \gamma^2 h_{\min,K}^2 p_E^3}{(h_{E,K}^\perp)^3} \right) \left\| \phi_h \right\|_{0,E}^2, \end{aligned}$$

with F_h and G_h are the L^2 projection of F and G respectively onto the finite element space. Here, A_{\min} and A_{\max} are the matrices constructed taking respectively the minimum and the maximum component by component of the definitions of A from the two elements sharing a face and

$$\alpha_K = \min \left(h_{\min,K} A^{-\frac{1}{2}} p_K^{-1}, \kappa_{\min}^{-\frac{1}{2}} \right), \quad \alpha_E = \min \left(h_{\min,K}^2 A_{\min}^{-\frac{1}{2}} p_E^{-1} \left(h_E^\perp \right)^{-1}, \kappa_{\min}^{-\frac{1}{2}} \right),$$

where κ_{\min} is the minimum value of κ_k on the computational domain Ω , $\|\cdot\|_{0,K}$ and $\|\cdot\|_{0,E}$ are respectively the L^2 -norm on an element K and on an edge E .

Adopting similar analysis from [15] it is possible to prove that the error estimator is an upper bound for the reference error in the DG norm $\|\cdot\|_{\mathcal{T}}$ i.e.,

$$\|\phi - \phi_h\|_{\mathcal{T}} \leq C (\eta_{\text{err}} + \Theta),$$

where C is a positive constant independent of the mesh nor the order of the elements used and

$$\Theta = \sqrt{\sum_{K \in \mathcal{T}} \frac{h_{\min,K}^2}{A_{\min} p_K^2} \left\| F - F_h \right\|_{0,K}^2 + \sum_{E \in \mathcal{E}^{BC}(\mathcal{T})} \frac{h_{\min,K}^2}{A_{\min} p_E^2 h_{E,K}^\perp} \left\| G - G_h \right\|_{0,E}^2},$$

is the data oscillations. Note that in case of SP₁ and SP₃ equations, the DG norm is defined as

$$\|\|u\|\|_{\mathcal{T}} = \left(\sum_{K \in \mathcal{T}} \left(A \left\| \nabla u \right\|_{L^2(K)}^2 + B \left\| u \right\|_{0,K}^2 \right) + \sum_{E \in \mathcal{E}^{int}(\mathcal{T})} \frac{\gamma 2\omega^+ A^+ p_E^2}{h_E^\perp} \left\| [u] \right\|_{0,E}^2 + \sum_{E \in \mathcal{E}^{BC}(\mathcal{T})} \frac{AD}{C} \left\| u \right\|_{0,E}^2 \right)^{1/2}.$$

In the present study, numerical implementation of the error estimator η_{err} is carried out using the `AptoFEM` software package. The resulting discrete systems of linear equations are solved by exploiting the Multifrontal Massively Parallel Solver (MUMPS), see for example [2–4]. We consider different adaptive techniques for the SP_1 and SP_3 approximations, namely: isotropic h -adaptivity, isotropic hp -adaptivity, anisotropic h -adaptivity, anisotropic h isotropic/ p -adaptivity and uniform h -adaptivity. In all our computations, the meshes are adapted by marking the elements for refinement according to the size of the local error indicators (3.11). This is achieved by employing the fixed fraction strategy proposed in [16], with a refinement fraction of 15%. Thus, for each element $K \in \mathcal{T}$ marked for refinement the schemes automatically decide whether the local mesh size h_K or the local polynomial degree p_K should be adjusted accordingly. The choice to perform either h - or p -refinement is based on estimating the local smoothness of the (unknown) analytical solution. To this end, we employ the hp -adaptive strategy developed in [17], where the local regularity of the analytical solution is estimated from truncated local Legendre expansions of the computed numerical solution. Furthermore, if anisotropic h -refinement is considered in the scheme, there is a further choice to make for each element qualified for refinement in h between isotropic h -refinement or anisotropic h -refinement. In order to make this choice we denote by $\mathcal{E}_K^1, \mathcal{E}_K^2$ the two sets containing opposite edges of the element K , and we define

$$\eta_{\mathcal{E}_K^i} = \sqrt{\eta_{E,K}^2|_{\mathcal{E}_K^i} + \eta_{B,K}^2|_{\mathcal{E}_K^i} + \eta_{J,K}^2|_{\mathcal{E}_K^i}}, \quad i = 1, 2.$$

Then the choice between isotropic h -refinement or anisotropic h -refinement is made comparing the error quantities $\eta_{\mathcal{E}_K^i}$ ($i = 1, 2$) as:

- (i) If $\eta_{\mathcal{E}_K^1} > 100\eta_{\mathcal{E}_K^2}$, then the element K is refined anisotropically along the direction \underline{v}_K^1 .
- (ii) If $\eta_{\mathcal{E}_K^2} > 100\eta_{\mathcal{E}_K^1}$, then the element K is refined anisotropically along the direction \underline{v}_K^2 .
- (iii) If none of the above conditions (i) and (ii) is satisfied, the element K is refined isotropically.

4 Numerical results

In this section we present numerical results for several test problems in frequency-dependent radiative transfer. The main goals of this section are to illustrate the numerical performance of the hp -adaptive discontinuous Galerkin method described above and to verify numerically its capabilities to solve radiative transfer problems. In all the computations reported herein, the media is assumed at a given steady temperature $T(x, y)$ and on the domain boundary the temperature $T_b(x, y)$ is fixed. The change between the media and the ambient temperatures causes a sharp drop in the temperature across a boundary layer which can be very thin depending on the physical properties of the media. As a thinner layer is considered the problem becomes more challenging to solve with the conventional finite element methods for which a very fine mesh is needed. To take this effect into consideration different values $\varepsilon = 0.5$, $\varepsilon = 0.1$ and $\varepsilon = 0.01$ are considered, which correspond to different optical regimes.

In the sequel, we shall use the terminology *isoh*, *isohp*, *anisoh*, *anisohisop* and *unifh* to refer to the DG method with, isotropic h -adaptivity, isotropic hp -adaptivity, anisotropic h -adaptivity, anisotropic h -adaptivity/isotropic p -adaptivity and uniform adaptivity, respectively. In addition, the resulting linear systems of algebraic equations are solved using the direct solver MUMPS. All the computations are performed on an Intel[®] Core i7 PC with 16 GB of RAM and 3.60 GHz. The codes only take the default optimization of the machine, *i.e.* they are not parallel codes.

4.1 Accuracy test problems

To assess the accuracy of the proposed adaptive DG method, we consider problems with known analytical solutions. We first solve the SP_1 problem in a grey unit squared domain using $\sigma = \kappa = 1$ and $r_1 = r_2 = 0$.

The functions F and G in the right-hand side of equations (3.1) are calculated such that the analytical solution of the SP₁ problem is given by

$$\varphi(x, y) = \left(\frac{e^{\frac{x-1}{A}} - 1}{e^{-\frac{1}{A}} - 1} + x - 1 \right) \left(\frac{e^{\frac{y-1}{A}} - 1}{e^{-\frac{1}{A}} - 1} + y - 1 \right).$$

We solve this problem for two different values of the diffusion scale $\varepsilon = 0.5$ and $\varepsilon = 0.1$. Note that despite the above exact solution is smooth it may develop boundary layers on the domain boundary and stronger boundary layers are expected for smaller values of ε .

In Figure 4.1 we present the convergence of the errors using different refinement techniques for both values of ε . It is clear that there is a huge difference between the adaptive techniques that involve p -refinement and the others that use only h -refinement. The formers converge exponentially whereas the others only polynomially. It should also be stressed that, due to the existence of the boundary layers in this example, the use of the anisotropic h -refinement seems to be advantageous for the DG method. It is also interesting to notice that for $\varepsilon = 0.1$, the boundary layers are stronger than the case with $\varepsilon = 0.5$ and the adaptive techniques which do not use anisotropic adaptivity are almost lost or they start to converge later. On the other hand, using anisotropic adaptivity the convergence is much faster and much sooner. For the considered diffusion scales, the anisohisop adaptivity achieves the fastest convergence for this test example compared to other adaptive techniques.

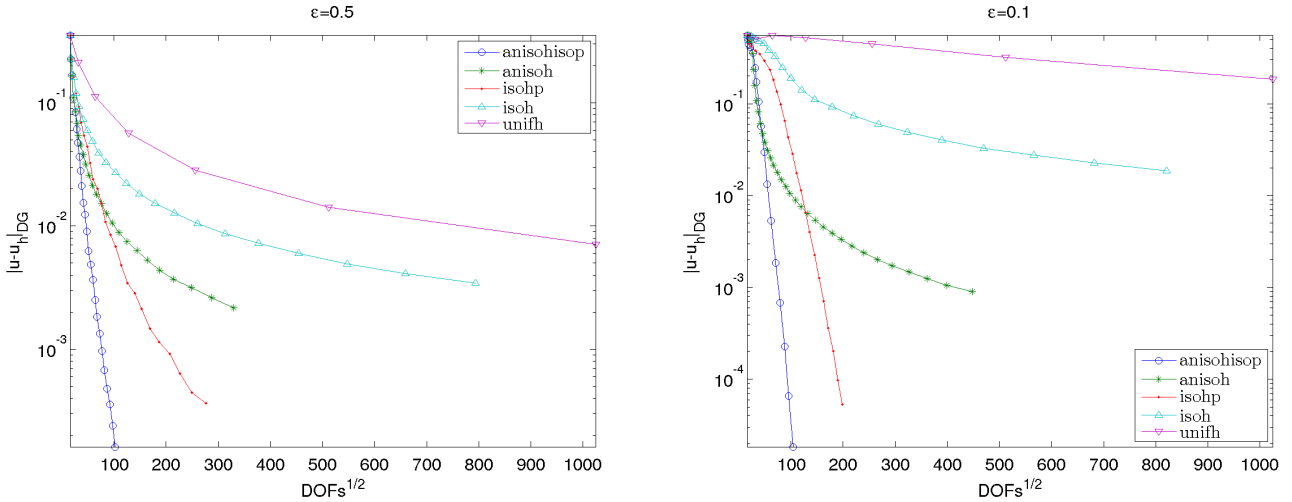


Figure 4.1: Convergence results in the DG norm using different refinement techniques for the accuracy test problem for the SP₁ model using $\varepsilon = 0.5$ (left) and $\varepsilon = 0.1$ (right).

In order to check how well the error estimator follows the true error, we illustrate in Figure 4.2 the two best cases from Figure 4.1, namely anisohisop and isohp along with the computed values of the estimator η_{err} . It is clear that the error estimator η_{err} follows very well the decay of the error in both cases which proves that it is a good estimation of the error. For both considered values of ε , the error estimator η_{err} is always an upper bound for the true error. Notice that the gap between the true value of the error and the error estimator is normal for this kind of error estimators as already analyzed in [15]. Figure 4.3 depicts the final adapted meshes using anisohisop. For a better visualization, only a zoom on the computational domain is shown in these plots. Note that the colors in the adapted meshes indicate the order of polynomials used in each element. As can be seen from these results the boundary layers have been accurately detected and treated using the anisotropic h -refinement as expected and accordingly to their strength.

Our second accuracy test example consists on solving the SP₃ equations with known analytical solution. Hence, we solve the equations (3.1) on a unit square using $\sigma = \kappa = 1$, $\alpha_1 = \alpha_2 = \beta_1 = \beta_2 = 1$ and

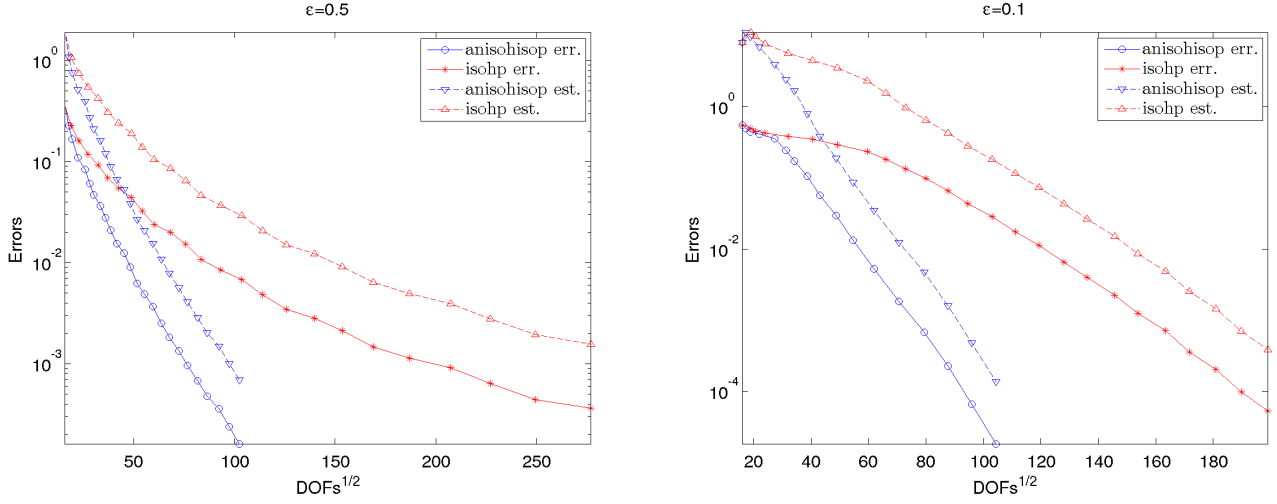


Figure 4.2: Comparison between the DG norm of the error and the error estimator for the accuracy test problem for the SP_1 model using $\varepsilon = 0.5$ (left) and $\varepsilon = 0.1$ (right).

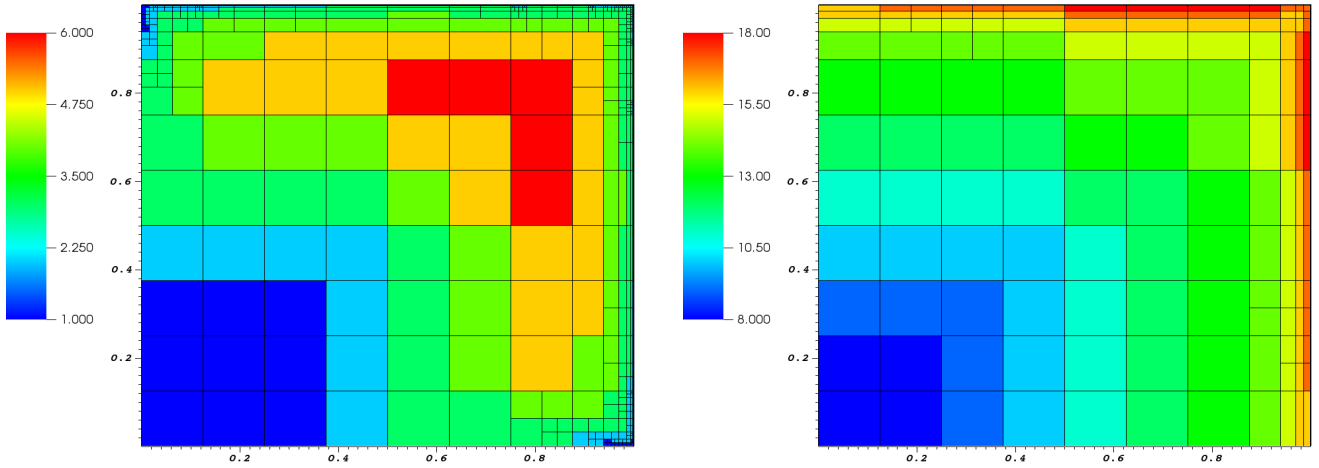


Figure 4.3: Adapted mesh using anisotropic h -refinement and isotropic p -refinement for the accuracy test problem for the SP_1 model using $\varepsilon = 0.5$ (left) and $\varepsilon = 0.1$ (right).

$\mu_1 = \mu_2 = 1$. The right-hand side F and boundary function G in (3.1) are analytically evaluated such that the exact solution of the SP_3 equations is

$$\begin{aligned} \psi_1(x, y) &= \left(\frac{e^{-\frac{x}{A}} - 1}{e^{-\frac{1}{A}} - 1} - x \right) \left(\frac{e^{-\frac{y}{A}} - 1}{e^{-\frac{1}{A}} - 1} - y \right), \\ \psi_2(x, y) &= \left(\frac{e^{\frac{x-1}{A}} - 1}{e^{-\frac{1}{A}} - 1} + x - 1 \right) \left(\frac{e^{\frac{y-1}{A}} - 1}{e^{-\frac{1}{A}} - 1} + y - 1 \right). \end{aligned}$$

Note that for this test example, the solution components ψ_1 and ψ_2 present boundary layers respectively, in the upper-right and lower-left regions of the computational domain. This problem is well-suited to test whether the indicator η_{err} is able to pick up the step gradients near these boundaries using anisotropic

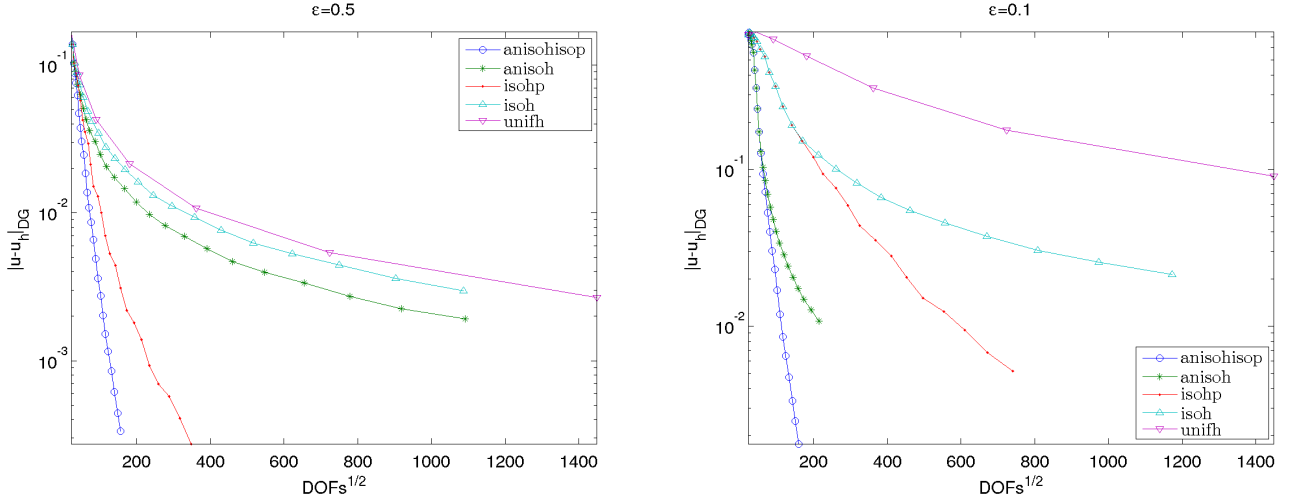


Figure 4.4: Convergence results in the DG norm using different refinement techniques for the accuracy test problem for the SP_3 model using $\varepsilon = 0.5$ (left) and $\varepsilon = 0.1$ (right).

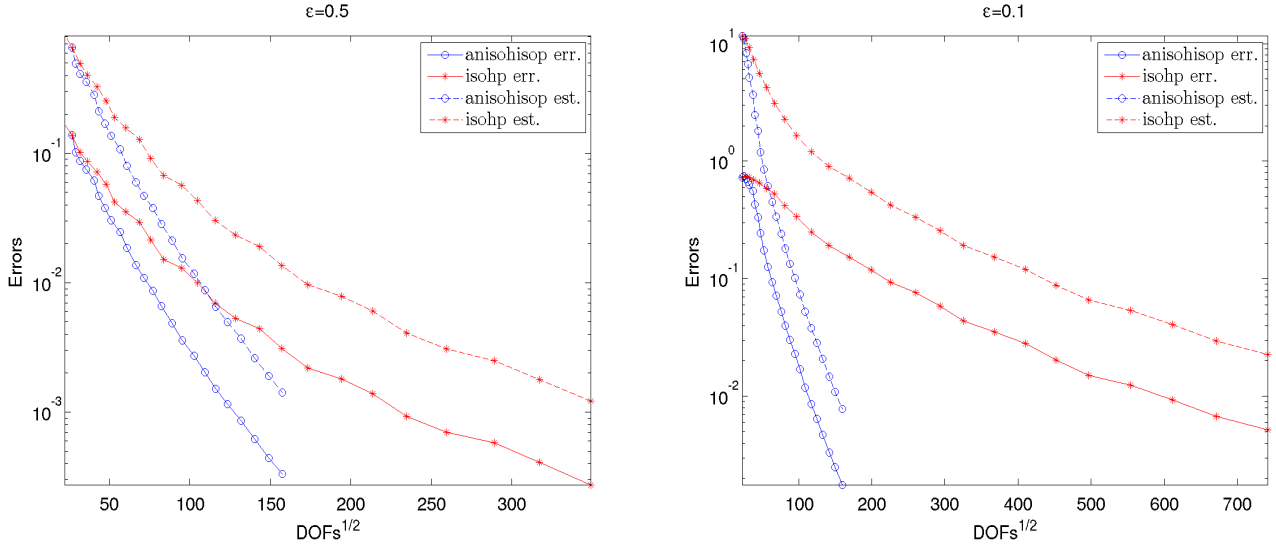


Figure 4.5: Comparison between the DG norm of the error and the error estimator for the accuracy test problem for the SP_3 model using $\varepsilon = 0.5$ (left) and $\varepsilon = 0.1$ (right).

refinement. As in the previous test problem, we consider the two radiative regimes associated with $\varepsilon = 0.5$ and $\varepsilon = 0.1$. Notice that all the numerical methods developed to solve the SP_3 equations solve ψ_1 and ψ_2 separately, see for example [18, 24]. In our approach the system is solved in a fully coupled manner and no iterations are needed to deal with boundary coupling between ψ_1 and ψ_2 .

Figure 4.4 presents the convergence results in the DG norm using different refinement techniques for $\varepsilon = 0.5$ and $\varepsilon = 0.1$. The corresponding error estimators for this problem are given in Figure 4.5. In the very beginning of iterations, the uniform and estimated errors are similar; however, we notice that the errors decrease generally during the evolving mesh adaptations while on the uniform grid the errors are evolved constantly. It is clear that for a given precision, the adaptive refinement allows to reduce consequently the number of unknowns in comparison with the uniform adaption. In addition, we note that both uniform refinements and adaptive refinements produce good approximate solutions as the number of degrees of

Table 4.1: Values of κ , σ and boundary functions for different tests in the verification test problems.

	σ	κ	$G_{\Gamma_l}(y)$	$G_{\Gamma_r}(y)$	$G_{\Gamma_b}(x)$	$G_{\Gamma_t}(x)$
Test 1	0.99	0.01	0	1	x	x
Test 2	99	1	0	1	x	x
Test 3	1	10	y	$1 - y$	x	$1 - x$

freedom increases, and the convergence orders are nearly optimal. However, to obtain similar accuracy, the adaptive refinements will use less finite elements. It should also be noted that the discrepancy between the true and estimated errors is remarkably small as compared to the magnitude of the target functional. The distribution of error contributions reflects the qualitative behavior of local errors and indicates that stronger mesh refinement is required in the vicinity of domain boundary as the diffusion scale ε increases. It is also worth pointing out that the boundary layers for this test example are adapted similarly to those reported in Figure 4.3 for the SP₁ equations and, for brevity in presentation, are not presented here.

4.2 Verification test problems

To assess the performance of the proposed DG method compared to the full radiative transfer, we consider a class of examples by solving the SP₁ and SP₃ approximations in a non-reflective grey unit square $\Omega = [0, 1] \times [0, 1]$ with $F = 0$. The boundary functions G in these test examples are defined as

$$\begin{aligned} G(0, y) &= G_{\Gamma_l}(y), & G(1, y) &= G_{\Gamma_r}(y), & \text{for } 0 \leq y \leq 1, \\ G(x, 0) &= G_{\Gamma_b}(x), & G(x, 1) &= G_{\Gamma_t}(x), & \text{for } 0 \leq x \leq 1. \end{aligned}$$

The coefficients κ , σ , the functions G_{Γ_l} , G_{Γ_r} , G_{Γ_b} and G_{Γ_t} are chosen for three different test problems according to Table 4.1. Similar test examples have been reported in [24]. Notice that since in these cases the analytical solutions are not available, we only present the decay of the error estimator η_{err} for each test example. However, as has been clearly shown in the previous test problems with known exact solutions, the error estimator mimics very well the behavior of the reference error and it is always an upper bound for this error in all optical regimes. This should give us the confidence in the fact that also the true error is decaying in a similar way as the error estimator for these problems. Figure 4.6 presents the convergence results of the error estimator in the DG norm using different refinement techniques for the three test examples using the SP₁ approximation with $\varepsilon = 0.1$ and $\varepsilon = 0.01$. Those results obtained using the SP₃ approximation are presented in Figure 4.7.

It is clear that, since the solution of **Test 1** does not present any strong boundary layers for the SP₁ approximation, anisotropic refinement would not give any advantage to the DG method. Clearly the trajectories of with or without anisotropic h -refinement for **Test 1** are exactly the same. This is due to the fact that also when the anisotropic h -refinement is available, the method automatically prefers the isotropic h -refinement in this case. However, for the SP₃ approximation of this test example, the anisotropic refinement gives some advantages to the DG method. The corresponding mesh statistics and CPU times for **Test 1** are summarized in Table 4.2 for both diffusion scales. Here the listed CPU time includes the computational time used to assemble the system, to solve this system and to compute the error estimator. It is clear that for this test example more degrees of freedom are needed for simulations using $\varepsilon = 0.01$ than those using $\varepsilon = 0.1$. The convergence in this later case is also slower compared to the case with $\varepsilon = 0.01$. Similar trends have been observed for results, not reported here, for the SP₃ approximation. For **Test 2** the solution presents very strong boundary layers along three sides of the computational domain. In this case anisotropic h -refinement has delivered a very fast convergence, compare the results shown in Figure 4.6 and Figure 4.7. The mesh statistics and CPU times for **Test 2** are also summarized in Table 4.3. *It should be noted that at early stage of simulation the advantage of p -refinement is limited for this test example,*

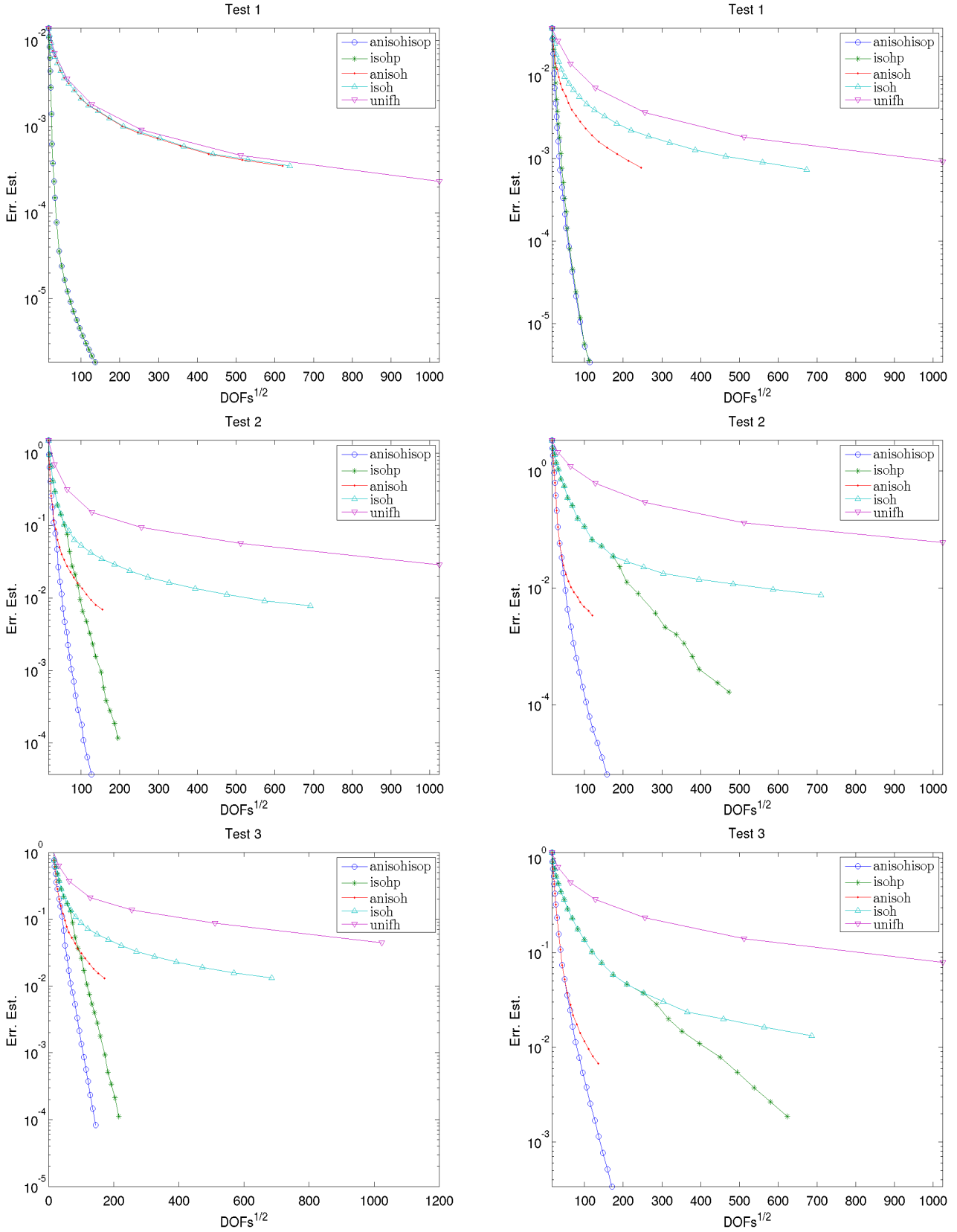


Figure 4.6: Convergence results in the DG norm using different refinement techniques for the three test examples in the verification test problems using the SP_1 approximation with $\varepsilon = 0.1$ (left column) and $\varepsilon = 0.01$ (right column).

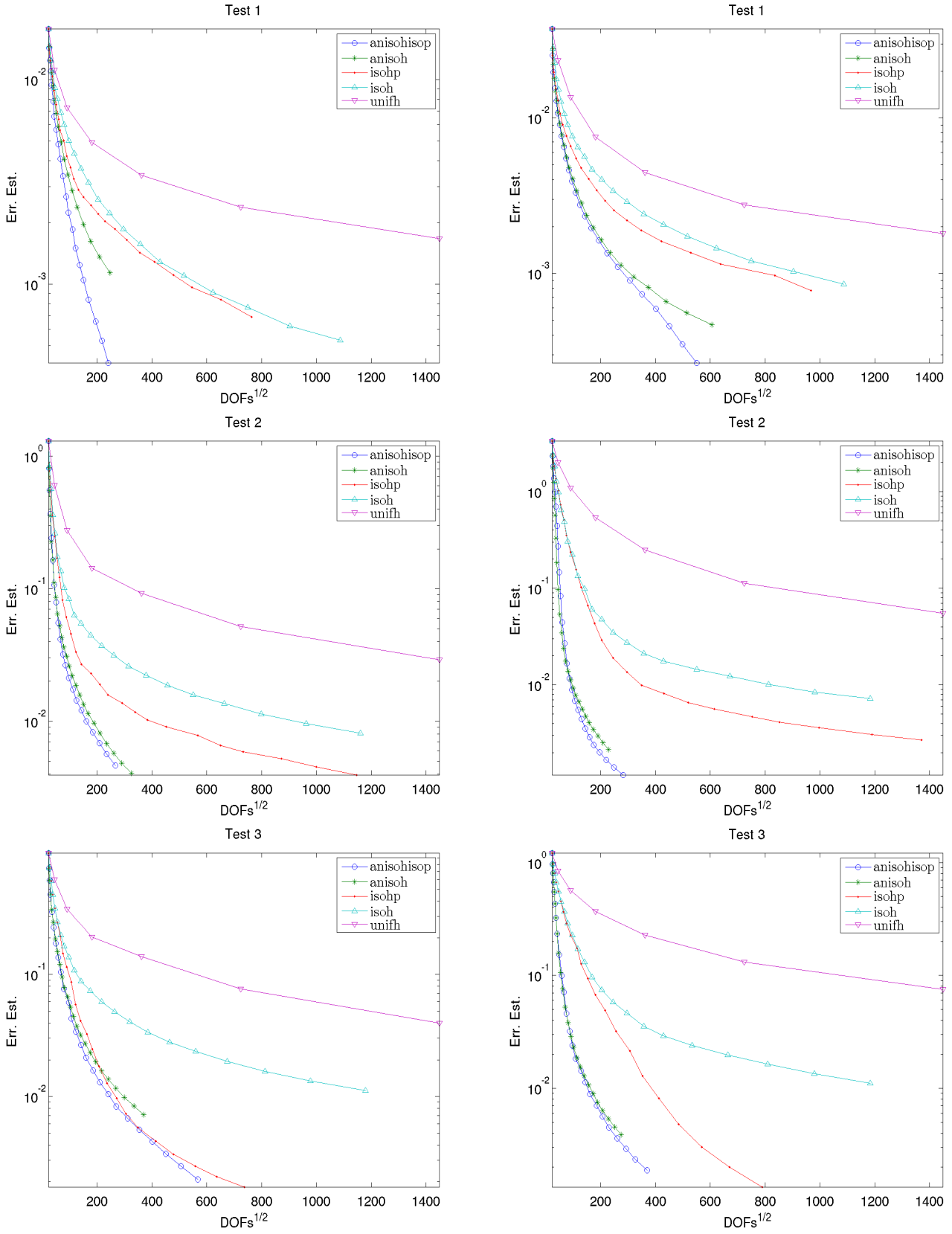


Figure 4.7: Same as Figure 4.6 but using the SP_3 approximation.

but it becomes very important later in the simulation. This happens very often in presence of boundary layers in the solution because at the beginning the h -refinement reduces much faster the error, but after the p -refinement is necessary to continue converging very quickly. This can be seen by examining the couples anisohisop/anisoh and isohp/isoh refinements.

Table 4.2: Mesh statistics, convergence results and computational times for SP_1 approximation of **Test 1** using $\varepsilon = 0.1$ and $\varepsilon = 0.01$. The CPU times are given in seconds.

Mesh	$\varepsilon = 0.1$				$\varepsilon = 0.01$			
	# Elems	# DoFs	η_{err}	CPU	# Elems	# DoFs	η_{err}	CPU
1	64	256	1.3979E-02	0.0091	64	256	3.8346E-02	0.0081
2	64	301	1.0832E-02	0.0078	77	318	2.8087E-02	0.0082
3	64	346	8.4505E-03	0.0075	84	386	1.8699E-02	0.0086
4	64	391	6.3190E-03	0.0091	86	468	1.0758E-02	0.0123
5	64	436	4.4319E-03	0.0289	94	540	7.1909E-03	0.0403
6	64	491	2.8531E-03	0.0387	94	674	4.6571E-03	0.0838
7	64	564	1.3970E-03	0.0546	108	792	3.2266E-03	0.0890
8	64	627	6.2494E-04	0.0615	114	898	2.3721E-03	0.1022
9	64	724	3.7774E-04	0.0750	122	1051	1.6219E-03	0.1203
10	64	938	2.3122E-04	0.1114	128	1259	1.0646E-03	0.1559
11	64	1070	1.4875E-04	0.1420	140	1410	7.2542E-04	0.1778
12	64	1354	7.7146E-05	0.1939	146	1832	4.4814E-04	0.2752
13	64	1864	3.5930E-05	0.3406	158	1993	3.3336E-04	0.3019
14	64	2510	2.3879E-05	0.5952	164	2528	2.1258E-04	0.4633
15	64	3332	1.6549E-05	1.0574	172	2702	1.4507E-04	0.4951
16	64	4256	1.2181E-05	1.1823	178	3526	8.5187E-05	0.7843
17	64	5344	9.2216E-06	2.1565	184	4706	4.2266E-05	1.2863
18	64	6560	7.1458E-06	2.4872	193	6187	2.1294E-05	1.9175
19	64	7904	5.6471E-06	4.9827	203	8011	1.0476E-05	2.0939
20	64	9376	4.5382E-06	5.8862	209	10237	5.2391E-06	2.6486
21	64	10976	3.7006E-06	8.3023	209	12909	3.3953E-06	5.8324
22	64	12704	3.0562E-06	12.1656	209	15975	2.6841E-06	7.2831
23	64	14560	2.5525E-06	14.7538	209	19446	2.1933E-06	10.6942
24	64	16544	2.1532E-06	19.5522	209	23287	1.8251E-06	16.3449
25	64	18656	1.8328E-06	27.2656	209	27694	1.5390E-06	24.0526

To further emphasis the high resolution of our DG method to resolve boundary layers for this problem we present in Figure 4.8 and Figure 4.9 the results obtained for **Test 2** using $\varepsilon = 0.1$ and $\varepsilon = 0.01$, respectively. Here we display the computed radiative mean intensity φ and the corresponding anisotropically adapted meshes. For better insight only small part of the computational domain is presented in these figures. As can be seen in these figures a thinner boundary layer is detected in the case using $\varepsilon = 0.01$ than using $\varepsilon = 0.1$ and in both situations our adaptive DG method accurately resolves these radiative regimes. It is worth remarking the degree of p -refinement in each case as higher polynomial degrees are needed for the case using $\varepsilon = 0.1$ than using $\varepsilon = 0.01$. Asymptotically, the size of these boundary layers should be proportional to ε^2 and our hp -adaptive DG method is able to accurately capture these boundary layers at reasonable computational cost. A simple examination of the number of degrees of freedom and the error estimator in Table 4.3 also reveals that larger number of degrees of freedom and faster convergence have been observed in the case using $\varepsilon = 0.01$ than using $\varepsilon = 0.1$.

Now we turn our attention to **Test 3** and for this test example, boundary layers appear in all four sides of the computational domain. However, these boundary layers are weaker than those appeared in the previous **Test 2**. Based on the results presented in Figure 4.6 and Figure 4.7 the anisotropic h -refinement achieves some advantages over other adaptive techniques. As in the previous test example, the results show a decrease in the error estimator as we increase the number of degrees of freedom in the system. The mesh statistics and CPU times for **Test 3** are also presented in Table 4.4. The obtained results for this example illustrate similar features to **Test 2**. Comparing the CPU times for the considered tests in this example it seems that **Test 1** is the most costly, this is due to the fact that in **Test 1** there is more p -adaptivity

Table 4.3: Mesh statistics, convergence results and computational times for SP_1 approximation of **Test 2** using $\varepsilon = 0.1$ and $\varepsilon = 0.01$. The CPU times are given in seconds.

Mesh	$\varepsilon = 0.1$				$\varepsilon = 0.01$			
	# Elems	# DoFs	η_{err}	CPU	# Elems	# DoFs	η_{err}	CPU
1	64	256	1.5063E-00	0.0085	64	256	3.3784E-01	0.0076
2	77	308	9.4895E-01	0.0063	77	308	2.4459E-01	0.0073
3	88	352	6.3489E-01	0.0077	92	368	1.8345E-01	0.0076
4	111	444	4.0510E-01	0.0058	105	420	1.3450E-01	0.0086
5	135	540	2.5413E-01	0.0111	120	480	9.3897E-01	0.0100
6	177	718	1.7896E-01	0.0542	142	568	6.3366E-01	0.0402
7	211	874	1.1115E-01	0.0834	169	676	3.7967E-01	0.0593
8	273	1177	7.7736E-02	0.1125	206	824	2.1087E-01	0.0759
9	308	1466	4.7046E-02	0.1522	254	1016	1.1061E-01	0.0879
10	322	1754	2.6798E-02	0.1781	330	1320	5.8088E-02	0.1151
11	338	2051	1.6907E-02	0.2275	416	1699	3.2812E-02	0.1652
12	352	2508	1.1431E-02	0.2758	474	2086	1.8087E-02	0.1998
13	353	2848	7.1922E-03	0.3104	524	2576	9.1560E-03	0.2720
14	381	3305	4.6886E-03	0.4003	544	3212	4.2720E-03	0.3285
15	456	3934	3.3986E-03	0.4830	603	4241	2.1462E-03	0.4876
16	456	4405	2.2665E-03	0.5375	628	5148	1.1309E-03	0.6021
17	481	5078	1.5170E-03	0.7056	666	6370	6.2564E-04	0.8339
18	503	5691	1.0523E-03	0.8023	709	7522	3.5782E-04	1.0114
19	543	6656	7.0826E-04	1.0647	777	9108	1.9982E-04	1.0855
20	574	7371	4.4950E-04	0.9018	798	10778	1.1091E-04	1.2494
21	611	8616	2.8657E-04	1.2209	821	12758	6.2210E-05	1.7123
22	640	10431	1.7786E-04	1.2933	855	14858	3.8218E-05	1.6812
23	675	11447	1.0997E-04	1.2987	968	17764	2.2105E-05	1.9650
24	692	13453	6.4254E-05	1.9867	1045	21333	1.2376E-05	2.7641
25	724	16193	3.7168E-05	2.3051	1065	25072	6.4624E-06	3.4325

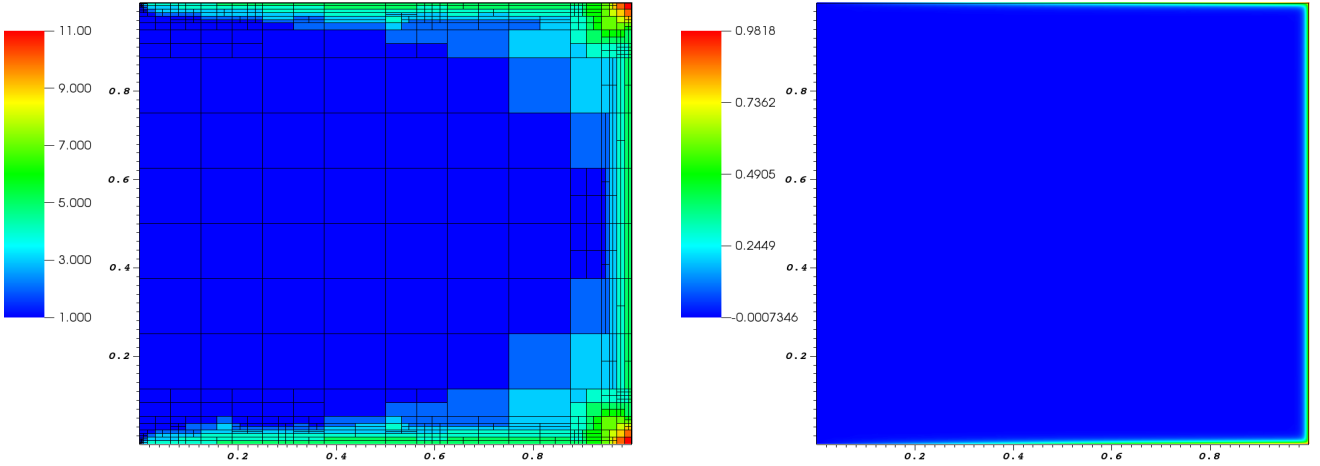


Figure 4.8: Adaptive mesh (left) and numerical solution (right) for the SP_1 approximation of **Test 2** using $\varepsilon = 0.1$. Colors in the adapted mesh indicate the order of polynomials used in each element.

than in the other cases. This leads to large dense blocks in the matrix of the linear systems which is a disadvantage when a direct solver is used as in this case.

Our final concern with this example is to compare the results obtained using the DG method for the simplified P_N models (3.1) to those from a direct solver for the full radiative transfer equation (2.1). To this

Table 4.4: Mesh statistics, convergence results and computational times for SP_1 approximation of **Test 3** using $\varepsilon = 0.1$ and $\varepsilon = 0.01$. The CPU times are given in seconds.

Mesh	$\varepsilon = 0.1$				$\varepsilon = 0.01$			
	# Elems	# DoFs	η_{err}	CPU	# Elems	# DoFs	η_{err}	CPU
1	64	256	1.0002E-00	0.0087	64	256	1.1524E-00	0.0079
2	77	308	7.5779E-01	0.0041	77	308	9.1746E-01	0.0060
3	92	368	6.0755E-01	0.0081	92	368	7.6523E-01	0.0071
4	121	484	4.7547E-01	0.0101	105	420	6.4204E-01	0.0094
5	145	580	3.5824E-01	0.0123	124	496	5.3155E-01	0.0104
6	189	756	2.8194E-01	0.0159	142	568	4.2354E-01	0.0420
7	271	1084	2.0071E-01	0.0740	172	688	3.2245E-01	0.0580
8	329	1366	1.5459E-01	0.1338	216	864	2.3375E-01	0.0737
9	400	1740	1.0973E-01	0.1683	278	1112	1.5818E-01	0.0945
10	444	2180	6.7907E-02	0.2330	359	1436	1.0852E-01	0.1210
11	479	2601	4.0467E-02	0.2722	457	1828	7.4276E-02	0.1546
12	506	3287	2.6295E-02	0.3716	597	2388	5.2746E-02	0.2021
13	522	3863	1.6885E-02	0.4377	731	3044	3.5569E-02	0.2893
14	568	4527	1.0963E-02	0.5128	909	3931	2.4549E-02	0.3715
15	679	5596	7.9720E-03	0.7088	1052	4872	1.6543E-02	0.5091
16	756	6692	5.2906E-03	0.8628	1226	6020	1.1377E-02	0.6521
17	800	7720	3.3405E-03	1.0031	1423	7599	7.7668E-03	0.8803
18	844	9030	2.1306E-03	1.1976	1614	9126	5.3718E-03	0.8385
19	880	10386	1.3558E-03	0.9642	1905	11200	3.7803E-03	0.9782
20	944	11768	8.5253E-04	0.9527	2076	13382	2.5535E-03	1.1173
21	1005	13325	5.6303E-04	1.3583	2327	16193	1.6928E-03	1.3366
22	1023	14913	3.7553E-04	1.5266	2542	18748	1.1421E-03	1.5243
23	1023	16646	2.3364E-04	1.5442	2818	21770	7.6463E-04	1.7505
24	1035	18512	1.4641E-04	1.7015	3087	25504	5.1686E-04	1.8113
25	1035	21099	8.2698E-05	1.8316	3286	29272	3.3928E-04	1.8570

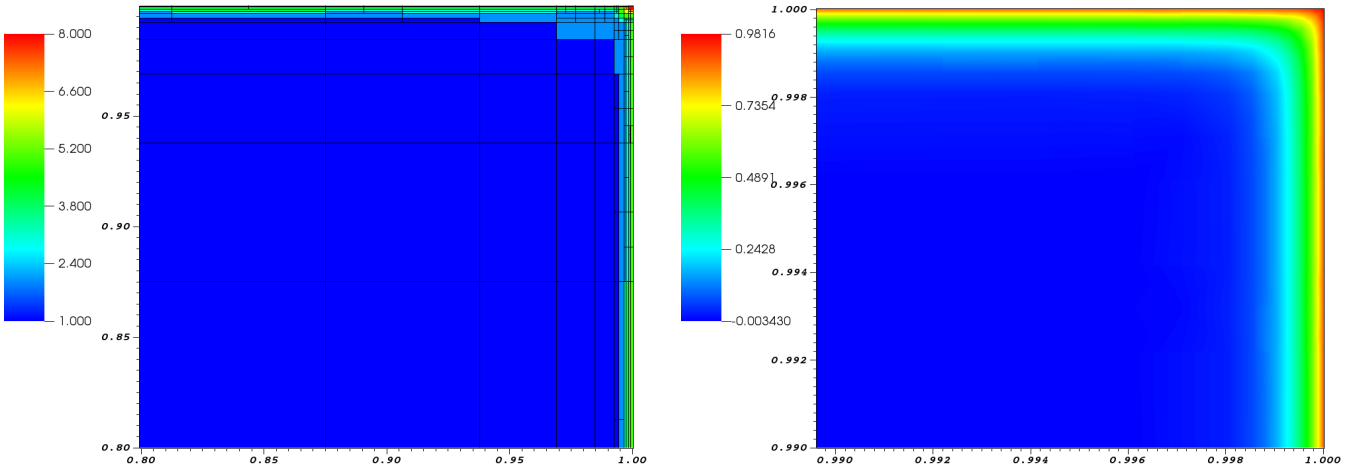


Figure 4.9: Same as Figure 4.8 but using $\varepsilon = 0.01$.

end we solve the radiative transfer equation (2.1) using the well-established Diffusion Synthetic Acceleration (DSA) method. The DSA method uses the diffusion approach to accelerate the source iteration which has been widely used in computational radiative transfer. We refer to [23, 24] for the implementation of the method and further discussions on other direct methods can be found therein. The S_8 discrete-ordinate algorithm is selected for the discretization of the angle variable and a mesh of 500×500 nodes for $\varepsilon = 0.1$

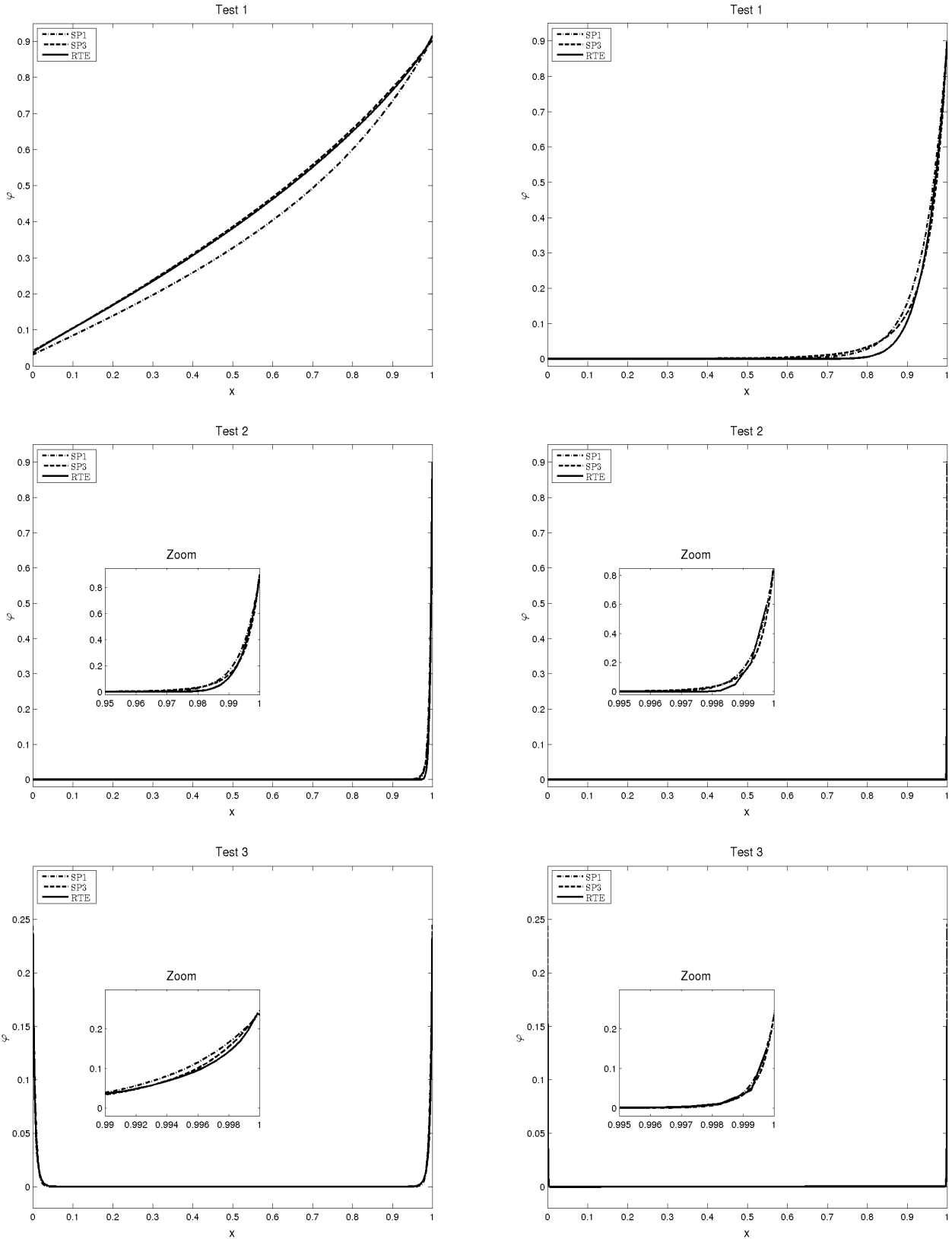


Figure 4.10: Comparison of cross-sections at $y = 0.5$ of the mean intensity for the three test examples in the verification test problems using $\varepsilon = 0.1$ (left column) and $\varepsilon = 0.01$ (right column).

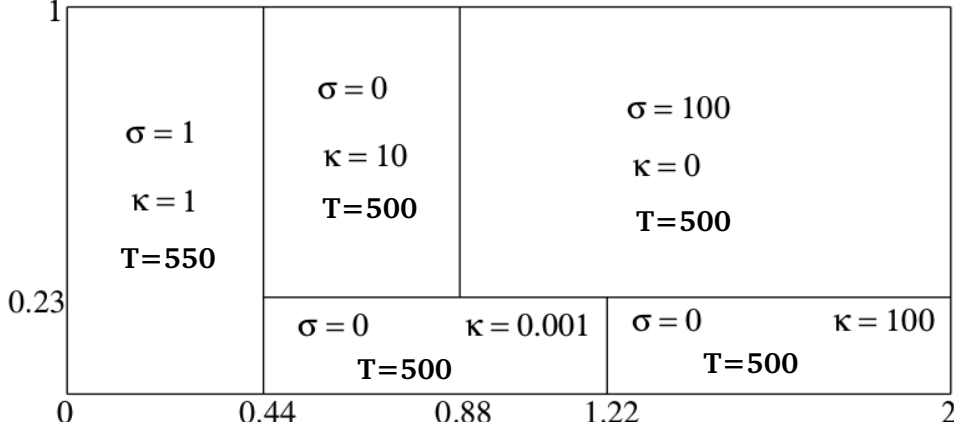


Figure 4.11: Computational domain and values of σ , κ and T in each sub-domain for the radiative transfer problem with discontinuous variables.

and 1000×1000 nodes for $\varepsilon = 0.01$ are used in our computations, yielding linear systems with 2×10^7 and 8×10^7 unknowns which has to be solved for the case with $\varepsilon = 0.1$ and $\varepsilon = 0.01$, respectively. In Figure 4.10 we present the cross-sections at $y = 0.5$ of the mean intensity φ obtained by the SP_1 and SP_3 approximations and the full radiative transfer for the three test problems from Table 4.1. It is evident that the proposed DG method preserves the radiative structures of the mean intensity at the optical regimes considered. The boundary features of the mean intensity are also captured by our DG method and they compare well with those obtained using the DSA solver for the full radiative transfer equation. It is also clear that the results obtained using the SP_1 and SP_3 approximations exhibit similar solution trends as the results obtained using the radiative transfer model. As reported in [24], the accuracy of the simplified P_N approaches and the convergence of the DSA method strongly depend on the optical scale ε and the scattering ratio $\gamma = \frac{\sigma}{\sigma + \kappa}$. Although, the scattering ratio is the same for **Test 1** and **Test 2** ($\gamma = 0.99$), a large discrepancy is detected in the results obtained using the DSA for SP_1 model for **Test 1**. It seems that, for the considered test cases, the simplified P_N approach asymptotically resolves the radiative transfer equation as the DSA method does, but with very less computational effort referring to the CPU times. It should be noted that when $\gamma \approx 1$ the DSA method converges slowly to a tolerance of 10^{-6} , for instance using $\varepsilon = 0.1$, in **Test 2** ($\gamma = 0.99$) the DSA method needs 1376 iterations to converge and in **Test 3** ($\gamma = 0.09$) it needs only 435 iterations. However, in all tests, the DG method for the SP_3 model shows fast convergence with a CPU time about 750 times lower than the DSA method for the full radiative transfer model.

4.3 Radiative transfer problem with discontinuous variables

The aim of this example is to test the performance of the proposed DG method for radiative transfer problems with discontinuous variables. Here, the problem statement consists on solving the SP_1 and SP_3 equations augmented by discontinuous temperature distribution, scattering and absorption coefficients. Note that for a grey media the Planck function (2.2) reduces to

$$B(T) = a_R T^4,$$

where $a_R = 5.67 \times 10^{-8}$ is the reduced Boltzmann constant. The domain geometry and the values of T , σ and κ for each sub-domain are illustrated in Figure 4.11. On the boundary the temperature is set to 300 K. A similar test example has also been considered in [1]. In Figure 4.12 we display the obtained radiative temperature using the SP_1 approximation with $\varepsilon = 0.1$ and $\varepsilon = 0.01$. Those results obtained using the SP_3 approximation are presented in Figure 4.13. Here, the radiative temperature T_R is obtained from the

thermal equilibrium

$$\varphi = 4\pi B(T_R),$$

where φ is the mean radiative intensity computed using either the SP₁ or SP₃ approximations. As expected steeper interface layers are present in the results obtained using $\varepsilon = 0.01$ compared to those obtained using $\varepsilon = 0.1$. These interface layers are more pronounced in the SP₁ than the SP₃ results. From the results shown in Figure 4.12 and Figure 4.13, our DG method has automatically detected these internal boundary layers and the meshes have been adapted consequently. It should also be pointed out that due to the selection of radiative parameters in the computational domain shown in Figure 4.11, the radiative temperature exhibits diffusive patterns in the right part of the computational domain which have been well detected by our DG method as more p -adaptivity is introduced in this part of the domain compared to the remaining parts in the computational domain. Note that sharper gradients have also been resolved using the SP₃ approximation for this test example compared to the SP₁ approximation. To further demonstrate this effect we present in Figure 4.14 cross-sections of the radiative temperature at $y = 0.5$ for both diffusive scales $\varepsilon = 0.1$ and $\varepsilon = 0.01$. It is evident that in the right part of the domain, the SP₁ and SP₃ approximations produce the same radiative temperatures. Furthermore, both values of ε yield similar results for SP₁ and SP₃ approximations. High resolution of boundary layers by our adaptive DG method should also be noted in the results presented in Figure 4.14. Although there is no available reference to quantitatively assess these solutions, it can be observed that the results are reasonable and consistent. In addition, the obtained results reveal the necessity of using hp -adaptation coupled with a *a posteriori* error estimate analysis for sophisticated radiation simulation quality enhancement. It is expected that for the considered radiative transfer problem, this procedure allows us to reach significant improvement in accuracy and stability, compared to the uniform adaptation, within a small number of iterations.

In summary, the adaptive DG method seems to produce satisfactory results and exhibit a typical high-resolution behavior for all the examples in the considered radiative regimes in grey media. Furthermore, the obtained results for the considered test examples demonstrate the ability of the presented adaptive DG method to capture the small solution features within the computational domain using low number of degrees of freedom and low computational cost without generating nonphysical oscillations at the interfaces or introducing excessive numerical diffusion in the numerical results.

4.4 Frequency-dependent radiative transfer problem

Our final test example is the problem of radiative transfer in combustion systems in which H_2O is the dominant radiating species. The full simulation of combustion systems requires the solution of the equations of material, momentum and enthalpy transport along with the radiative transfer equations. Since our focus in the current work is on developing efficient numerical solvers for radiative transfer, we will consider only the simplified P_N equations. The main aim of this example is to check the performance of the proposed hp -adaptive DG method for solving frequency-dependent radiative transfer problems in relatively complex domains. Here, we solve the SP₁ and SP₃ equations in a circular-shaped reactor with 2 m of radius. The domain boundary is maintained at the ambient temperature of $T_b = 300 K$ and the interior medium has a steady temperature exponentially decaying from 2500 K to 2000 K as

$$T(x, y) = 2000 + 500 \exp\left(-\frac{\sqrt{x^2 + y^2}}{0.08}\right).$$

In order to handle curved domains in this example, we have curved the elements using the transfinite interpolation method [25]. It should be noted that the visualization tool that we use to plot the meshes is not able to draw curved elements, so even if the elements are treated as curved in our DG method, in the displayed figures they have straight edges. The initial mesh used in our simulations is shown in Figure 4.15. As can be seen in the left plot of this figure, the mesh is constituted with both quadrilateral and triangular elements. Since we know already that boundary layers can appear along the domain boundary, quadrilateral elements have been chosen because they can easily be adapted anisotropically. In the interior

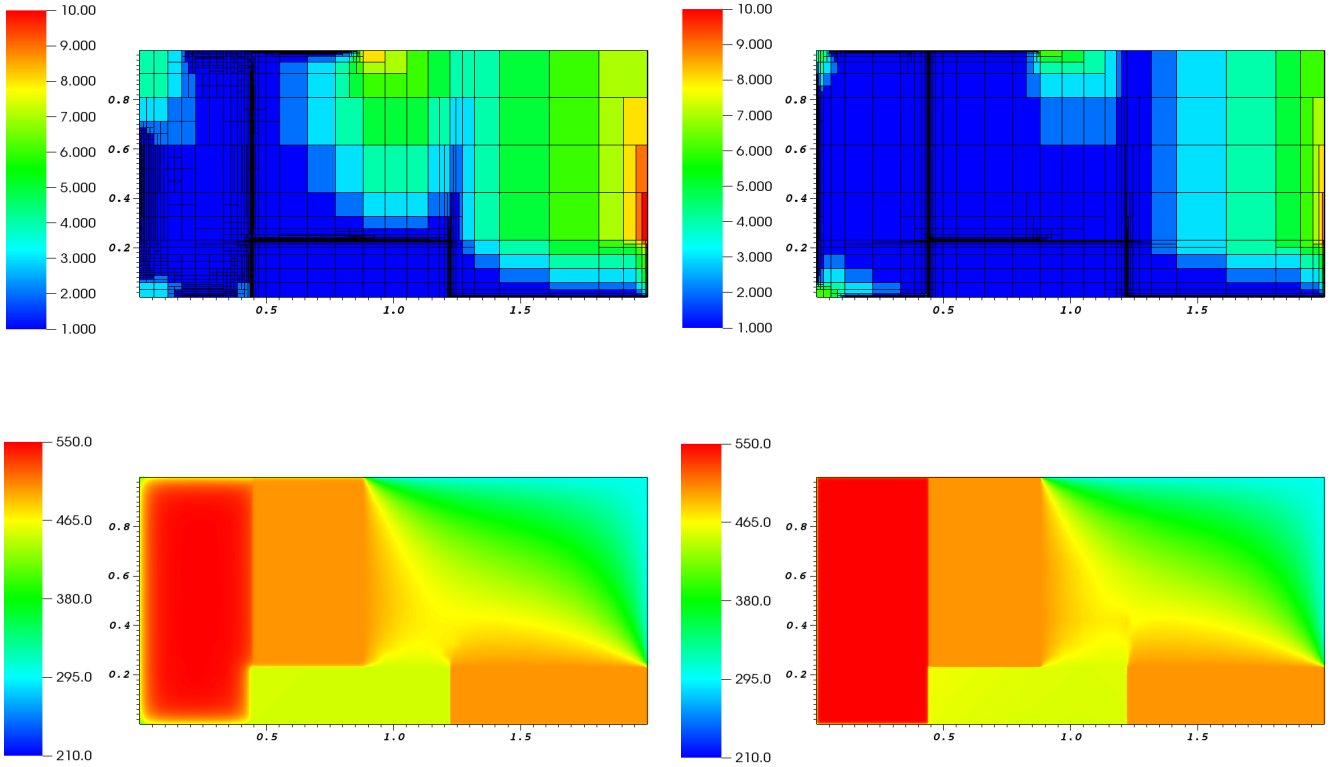


Figure 4.12: Adapted meshes (first row) and the associated radiative temperatures (second row) obtained for the SP_1 approximation using $\varepsilon = 0.1$ (left) and $\varepsilon = 0.01$ (right) for the problem with discontinuous variables. Colors in the meshes indicate the order of polynomials used in each element.

of the circular domain, triangular elements are used because they can describe any topology. The same approach can be used for any curved shape for computational radiative transfer in complex domains.

In Figure 4.15 we present the spectrum used in our computations for H_2O species [11]. The non-opaque frequency interval $[\nu_0, \infty)$ is approximated by 67 bands with piecewise constant absorption coefficients as shown in the right plot of Figure 4.15. Since the data are originally defined by wavelength intervals $[\lambda_{k-1}, \lambda_k]$, we computed the corresponding frequency bands using the relation

$$\nu_k = \frac{c_0}{\lambda_k n_m}, \quad k = 1, 2, \dots, 67,$$

where c_0 is the speed of light in vacuum. It is evident from this figure that the material is non-grey and the optical properties strongly change with the wavelength. In addition, H_2O is considered to be non-scattering and opaque to radiation for wavelengths larger than a cut-off wavelength equal to $16 \mu m$. In all the computations reported herein, we used $c_0 = 2.9979 \times 10^8 \text{ m/s}$, $h_P = 6.62608 \times 10^{-34} \text{ Js}$, $k_B = 1.38066 \times 10^{-23} \text{ J/K}$, $n_m = 1.33$ and $\varepsilon = 0.1$. In this study we highlight the effect of an instantaneous change in the ambient temperature from 2000 K to 300 K , causing a sharp drop in the temperature across a boundary layer that can be very thin depending on the physical properties of the enclosure. As a thinner layer is considered the problem becomes more challenging to solve with the conventional finite element methods.

Figure 4.16 shows the adaptive meshes and the mean radiative intensity φ for the selected bands 7, 18, 49 and 63 using the SP_1 approximation. The results obtained using the SP_3 approximation are shown in Figure 4.17. As can be seen from the results presented in these figures, the computed mean intensities

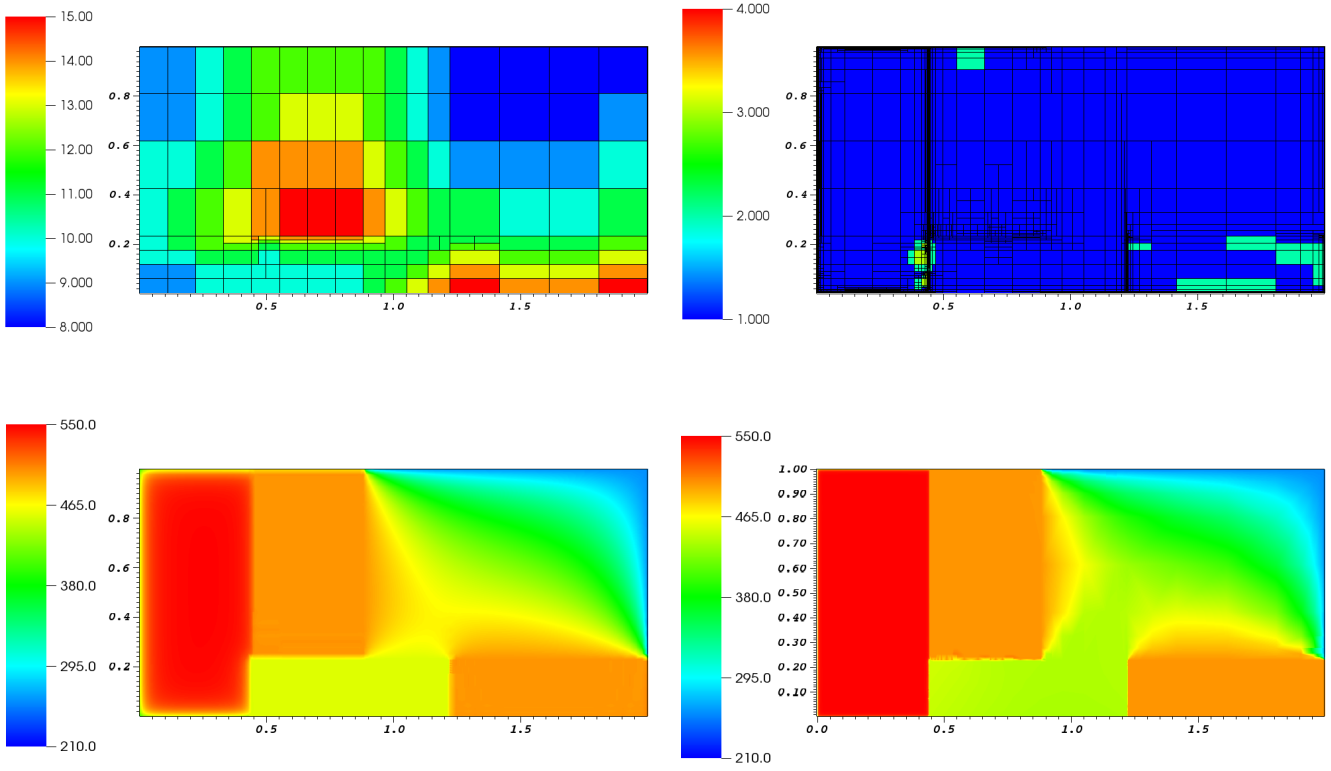


Figure 4.13: Same as Figure 4.12 but for the SP_3 approximation.

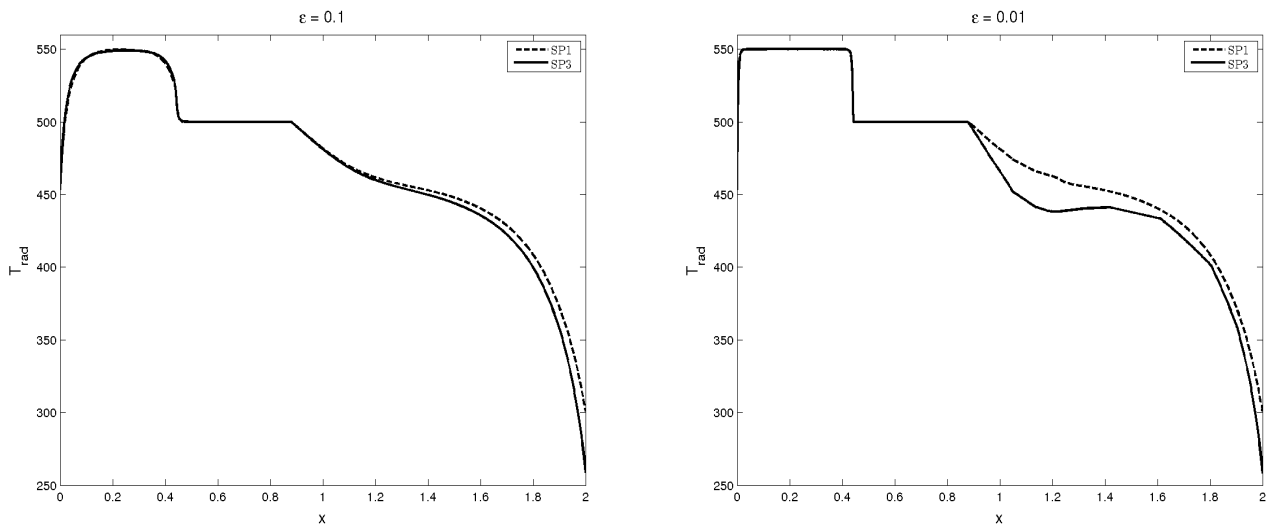


Figure 4.14: Cross-sections of the radiative temperature at $y = 0.5$ for the problem with discontinuous variables with $\varepsilon = 0.1$ (left) and $\varepsilon = 0.01$ (right).

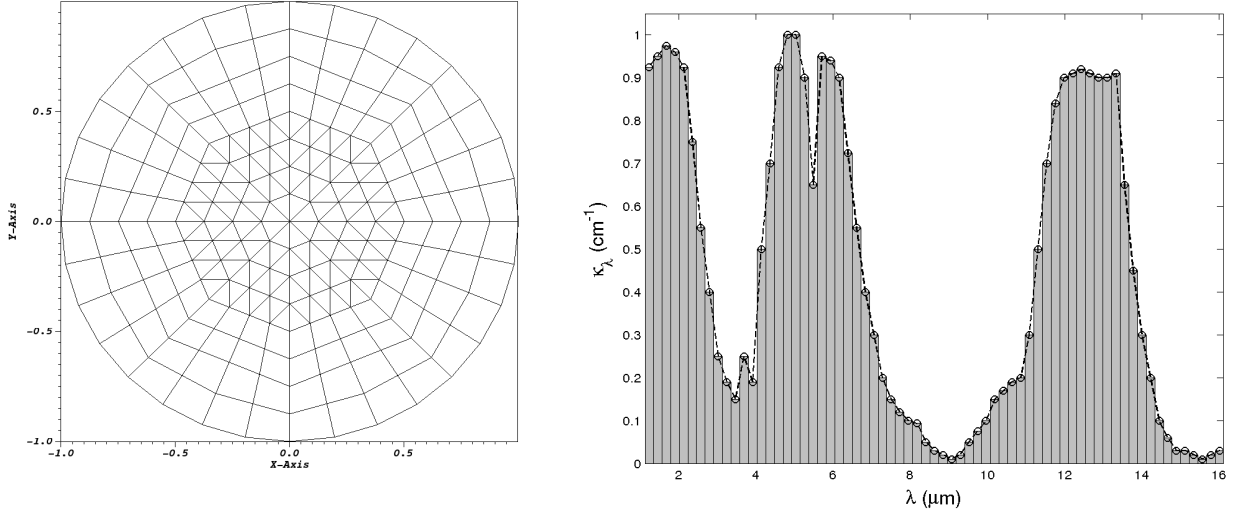


Figure 4.15: Initial mesh (left) spectral absorption coefficients κ for the species H_2O (right).

φ_k ($k = 7, 18, 49$ and 63) exhibit similar radiative patterns with highest intensity located in center of the domain and it decays exponentially to the ambient radiation. However, the speed of this decay and the thickness of the associated boundary layers differ from a band to another. For instance, faster decay and thicker boundary layer have been observed in the 63th band for φ_{63} compared to other bands in both simulations using SP_1 and SP_3 approximations. These features can be clearly seen in Figure 4.18 where radial cross-sections of mean intensities are performed along the main diagonal in the domain. These effects can be attributed to the absorption coefficients used in the simulation for each band in the radiative spectrum. It is also clear from Figure 4.18 that for the considered value of diffusion scale ε , no noticeable differences are visible between the SP_1 and SP_3 solutions for bands 7, 18 and 49. This also confirms the asymptotic analysis used to derive the SP_N approximations and one expects that for this class of simulations, solutions obtained using the full radiative transfer coincide with those obtained using the SP_3 approximation but at very heavy computational cost. Our numerical simulations demonstrate that the coupling of mesh adaptation and *a posteriori* error estimate allows for an economical and accurate DG solution of frequency-dependent radiative transfer problems.

In terms of adapted meshes shown in Figure 4.16 and Figure 4.17, it is evident that the *hp*-adaptation patterns are different for each band. It seems that for radiative transfer using H_2O species, high *p*-refinement is observed for boundary layers and low *p*-refinement for regions with high temperature. The *h*-refinement is also taken place inside the circular domain where the temperature reaches high values. It is clear that the proposed estimator locates the error very well and the maximum error is well captured at the boundary of the computational domain. In addition, for the considered radiative conditions, we can observe that the number of degrees of freedom differs from one band to another and the *hp*-adaptation is automatically switched on only when it is needed for the concerned band independently of the other bands, which confirms the relevance of the adaption criteria based on our error estimator. Finally, we summarize in Table 4.5 the number of degrees of freedom and the values of the error estimator on the first 10 adapted meshes for all four considered bands using the SP_1 approximation. As mentioned before, increasing the number of degrees of freedom results in a decrease in the error estimator. However, faster convergence can be seen for the 63th band compared to the other bands. It is worth remarking that the high values of the error estimator in this problem are related to the high values of the numerical solution itself. Similar conclusions can be drawn from results obtained using the SP_3 approximation and not reported here. Note that the performance of the proposed DG method is very attractive since the computed solutions remain stable and oscillation-free even for relatively coarse meshes without global refinement for all frequency bands within

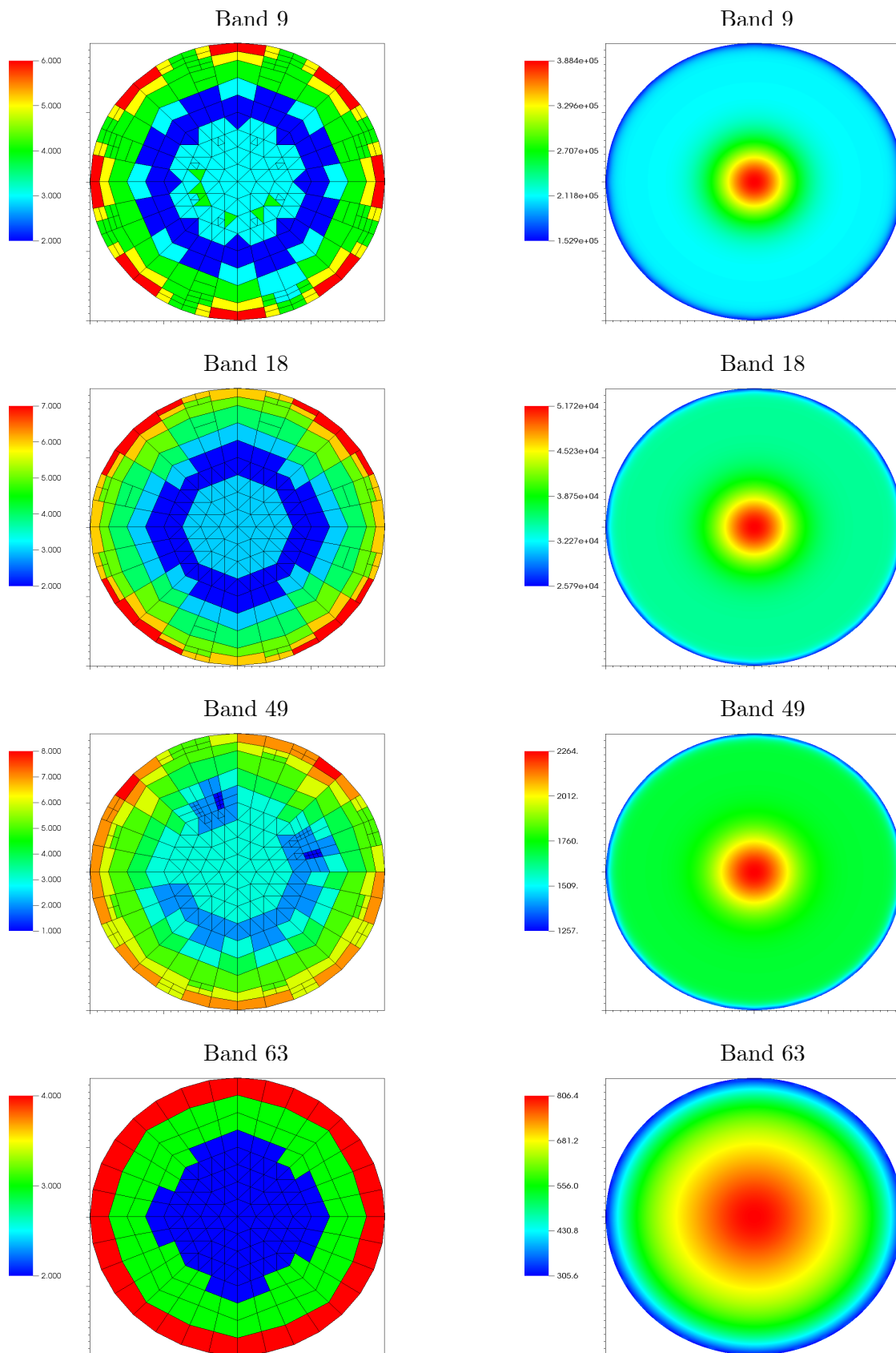


Figure 4.16: Adapted meshes (left column) and mean radiative intensity (right column) obtained for different frequency bands using SP_1 approximation of the frequency-dependent radiative transfer problem.

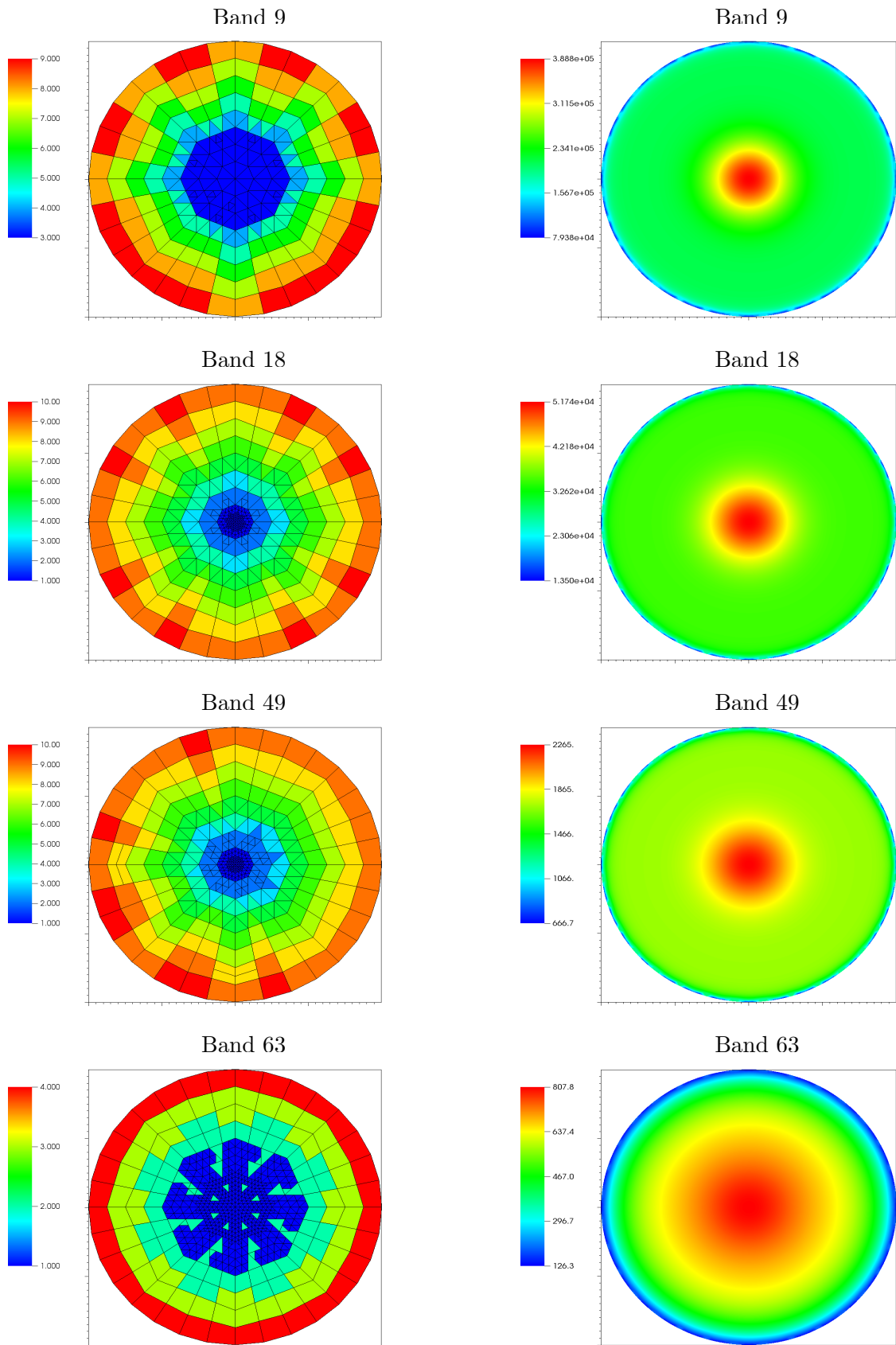


Figure 4.17: Same as Figure 4.16 but for the SP₃ approximation.

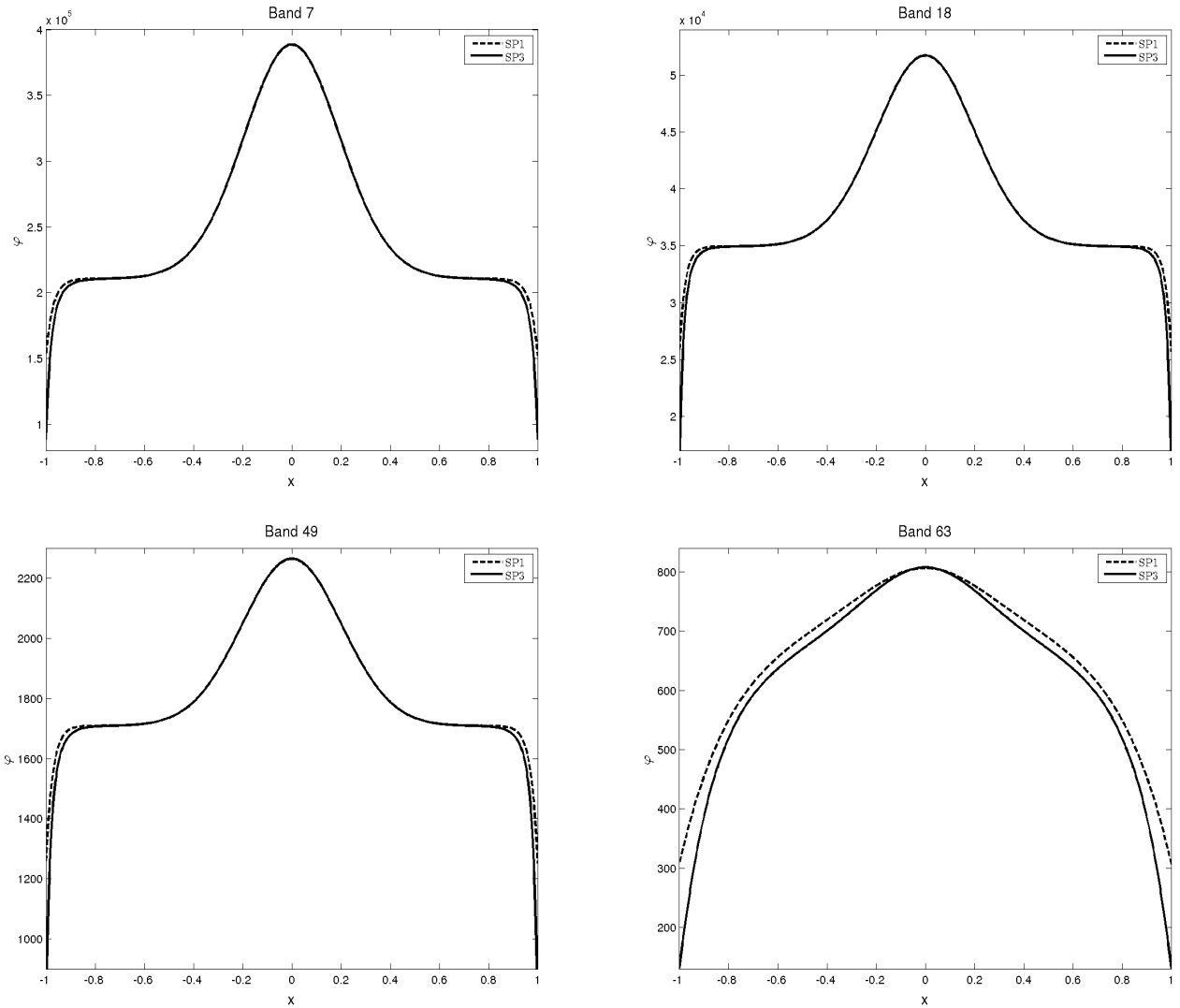


Figure 4.18: Radial cross-sections of mean intensities along the main diagonal for the four considered bands.

the radiative spectrum.

5 Conclusions

A robust class of hp -adaptive discontinuous Galerkin methods is proposed for the numerical solution of simplified P_N approximations of radiative transfer in non-grey semitransparent media. The integro-differential equation of radiative transfer is approximated by the simplified P_N equations resulting in a set of equations independent of directional coordinates and easy to be integrated in existing software packages. The proposed discontinuous Galerkin method is simple and highly accurate. The method is also locally conservative finite element method whose approximate solutions are discontinuous across inter-element boundaries; this property renders the method ideally suited for the hp -adaptivity. Numerical results are presented for several test problems in frequency-dependent radiative transfer and comparisons between different adaptivity procedures have been assessed. It has been found that it is possible to estimate the radiative field with a computational cost very significantly lower than solving the equations using the conventional finite element method. In addition, for optically thick media the simplified P_N approximations give results which are close

Table 4.5: Number of degrees of freedom and values of the error estimator on the first 10 adapted meshes for the four considered bands in the SP_1 approximation.

Band 7		Band 18		Band 49		Band 63	
DoFs	η_{err}	DoFs	η_{err}	DoFs	η_{err}	DoFs	η_{err}
896	73150.	896	13997.	896	617.77	896	86.600
1064	43174.	1064	8542.4	1070	368.20	1086	33.575
2097	18155.	1960	1545.4	2100	108.41	1276	14.334
2563	7045.5	2552	519.71	2578	33.099	1494	9.5181
3003	4023.0	3774	364.40	3642	14.748	1704	6.9688
3333	2803.8	4232	240.33	4318	9.5747	1856	4.6333
3626	1893.3	4400	139.71	4486	6.2435	2026	3.6051
4544	962.29	5056	79.821	5854	2.7802	2368	1.3987
6149	459.34	6104	43.898	7032	1.6925	2682	0.95094
7462	265.88	7446	32.114	9352	1.0422	2964	0.52663

to those computed by the full radiative transfer problem.

At present, we are trying to adapt this method to more difficult problems, such as those used in glass manufacturing. The equations in this model are strongly nonlinear and involve hydrodynamics and chemistry effects. We believe that these problems may benefit from the hp -adaptive discontinuous Galerkin method by reducing the number of degrees of freedom needed for convergence. However, this will require further study and a robust *a posteriori* error estimator may be required which is a topic of a forthcoming paper. It is worthwhile to remark that the presented hp -adaptive discontinuous Galerkin solver is designed in such a way that it can easily be integrated into an existing CFD code for hydrodynamical flow and heat mass transfer. Finally, we point out that the parallel implementation of the hp -adaptive discontinuous Galerkin method presented in this study is straightforward and only requires interprocessor communication to complete the matrix-vector and vector-vector products required for each frequency band.

A Appendix: Boundary condition for simplified P_N equations

Here we summarize the variables required in the boundary conditions for the SP_N approximations (2.7) and (2.8). For more details on the asymptotic analysis used to derive these conditions we refer the reader to [20]. Hence we define the integrals r_i , $i = 1, \dots, 7$ by

$$\begin{aligned}
 r_1 &= \int_0^1 \mu \varrho(-\mu) d\mu, & r_3 &= \int_0^1 \mu^3 \varrho(-\mu) d\mu, & r_6 &= \int_0^1 P_1(\mu) P_3(\mu) \varrho(-\mu) d\mu, \\
 r_2 &= \int_0^1 \mu^2 \varrho(-\mu) d\mu, & r_4 &= \int_0^1 \mu P_3(\mu) \varrho(-\mu) d\mu, & r_5 &= \int_0^1 P_3(\mu) \varrho(-\mu) d\mu, \\
 r_7 &= \int_0^1 P_3(\mu) P_3(\mu) \varrho(-\mu) d\mu,
 \end{aligned}$$

where ϱ is the reflectivity function given by (2.4), P_1 and P_3 are Legendre polynomials of order 1 and 3 defined as

$$P_1(\mu) = \mu, \quad P_3(\mu) = \frac{5}{2}\mu^3 - \frac{3}{2}\mu.$$

Hence, the parameters r_1 and r_2 required in (2.7) for the boundary condition of SP_1 approximation are given above. The constants appeared in (2.8) for the boundary condition of SP_3 approximation are listed as follows:

$$\begin{aligned}\mu_1^2 &= \frac{1}{7} \left(3 - 2\sqrt{\frac{6}{5}} \right), & \gamma_1 &= \frac{5}{7} \left(1 - 3\sqrt{\frac{6}{5}} \right), \\ \mu_2^2 &= \frac{1}{7} \left(3 + 2\sqrt{\frac{6}{5}} \right), & \gamma_2 &= \frac{5}{7} \left(1 + 3\sqrt{\frac{6}{5}} \right),\end{aligned}$$

$$\begin{aligned}\alpha_1 &= \frac{C_1 D_4 - C_4 D_1}{C_3 D_4 - D_3 C_4}, & \beta_1 &= \frac{C_3 D_1 - C_1 D_3}{C_3 D_4 - D_3 C_4}, & \eta_1 &= \frac{D_4 \rho_1 - C_4 \rho_3}{C_3 D_4 - D_3 C_4}, \\ \alpha_2 &= \frac{C_3 D_2 - C_2 D_3}{C_3 D_4 - D_3 C_4}, & \beta_2 &= \frac{C_2 D_4 - C_4 D_2}{C_3 D_4 - D_3 C_4}, & \eta_2 &= \frac{C_3 \rho_3 - D_3 \rho_1}{C_3 D_4 - D_3 C_4},\end{aligned}$$

where

$$\begin{aligned}A_1 &= \frac{1 - 2r_1}{4}, & B_1 &= -\frac{1 + 8r_5}{16}, & C_1 &= w_0(\gamma_2 A_1 - A_2), \\ A_2 &= \frac{5(1 - 8r_3)}{16}, & B_2 &= \frac{5(1 - 8r_6)}{16}, & C_2 &= w_0(-\gamma_1 A_1 + A_2), \\ A_3 &= \frac{1 + 3r_2}{6}, & B_3 &= \frac{3r_4}{6}, & C_3 &= w_0(\gamma_2 A_3 - A_4), \\ A_4 &= r_4 + \frac{2}{9}(1 + 3r_2), & B_4 &= r_4 + \frac{3}{14}(1 + 7r_7), & C_4 &= w_0(-\gamma_1 A_3 - A_4),\end{aligned}$$

$$D_1 = w_0(\gamma_2 B_1 - B_2), \quad D_3 = w_0(\gamma_2 B_3 - B_4),$$

$$D_2 = w_0(-\gamma_1 B_1 + B_2), \quad D_4 = w_0(-\gamma_1 B_3 + B_4),$$

with $w_0 = \frac{7}{36}\sqrt{\frac{6}{5}}$, ρ_1 and ρ_3 are given by

$$\rho_1 = (1 - 2r_1)\pi \quad \text{and} \quad \rho_3 = -\left(\frac{1}{4} + 2r_5\right)\pi.$$

Note that the above parameters depend only on the optical reflectivity of the material where the radiation has to be estimated. They can be calculated in advance and stored to be used whenever a simulation of solution has to be repeated in the frequency loop.

References

- [1] M.L. Adams and E.W. Larsen. Fast iterative methods for discrete-ordinates particle transport calculations. *Progress in Nuclear Energy*, 40:3–159, 2002.
- [2] P.R. Amestoy, I.S. Duff, J. Koster, and J.Y. L'Excellent. A fully asynchronous multifrontal solver using distributed dynamic scheduling. *SIAM Journal on Matrix Analysis and Applications*, 23:15–41, 2001.
- [3] P.R. Amestoy, I.S. Duff, and J.Y. L'Excellent. Multifrontal parallel distributed symmetric and unsymmetric solvers. *Comput. Methods Appl. Mech. Eng.*, 184:501–520, 2000.
- [4] P.R. Amestoy, A. Guermouche, J.Y. L'Excellent, and S. Pralet. Hybrid scheduling for the parallel solution of linear systems. *Parallel Computing*, 32:136–156, 2006.
- [5] D.N. Arnold, F. Brezzi, B. Cockburn, and L.D. Marini. Unified analysis of discontinuous Galerkin methods for elliptic problems. *SINUM*, 39:1749–1779, 2002.

- [6] R. Backofen, T. Bilz, A. Ribalta, and A. Voigt. SP_N -approximations of internal radiation in crystal growth of optical materials. *J. Crystal Growth.*, 266:264–270, 2004.
- [7] F. Bassi and S. Rebay. A high-order accurate discontinuous finite element method for the numerical solution of the compressible Navier-Stokes equations. *J. Comput. Phys.*, 131(2):267–279, 1997.
- [8] F. Bassi and S. Rebay. High-order accurate discontinuous finite element solution of the 2D Euler equations. *Journal of Computational Physics*, 138(2):251–285, December 1997. ACM ID: 274113.
- [9] A. Buffa and I. Perugia. Discontinuous Galerkin Approximation of the Maxwell Eigenproblem. *SIAM Journal on Numerical Analysis*, 44(5):2198, 2006.
- [10] E. Burman and A. Ern. Continuous Interior Penalty hp-Finite Element Methods for Advection and Advection-Diffusion Equations. *Mathematics of Computation*, 76(259):1119–1140, 2007.
- [11] P. Cumber, M. Fairweather, and H. Ledint. Application of wide band radiation models to nonhomogeneous combustion systems. *Int. J. Heat Mass Transfer*, 41:1573–1584, 1998.
- [12] C. Farhat, I. Harari, and U. Hetmaniuk. A discontinuous Galerkin method with Lagrange multipliers for the solution of Helmholtz problems in the mid-frequency regime. *Computer Methods in Applied Mechanics and Engineering*, 192:1389–1419, 2003.
- [13] M. Frank, M. Seaid, J. Janicka, A. Klar, R. Pinnau, and G. Thömmes. A comparison of approximate models for radiation in gas turbines. *Int. J. Progress in CFD*, 3:191–197, 2004.
- [14] E.M. Gelbard. *Simplified Spherical Harmonics Equations and their Use in Shielding Problems*. Technical Report WAPD-T-1182, Bettis Atomic Power Laboratory, 1961.
- [15] S. Giani, D. Schötzau, and L. Zhu. An a-posteriori error estimate for hp -adaptive DG methods for convection–diffusion problems on anisotropically refined meshes. *Computers & Mathematics with Applications*, 67:869–887, 2014.
- [16] P. Houston and E. Süli. Adaptive finite element approximation of hyperbolic problems. *Lect. Notes Comput. Sci. Engrg.*, 25:269–344, 2002.
- [17] P. Houston and E. Süli. A note on the design of hp -adaptive finite element methods for elliptic partial differential equations. *Computer Methods in Applied Mechanics and Engineering*, 194:229–243, 2005.
- [18] A. Klar, J. Lang, and M. Seaid. Adaptive solutions of SP_N -approximations to radiative heat transfer in glass. *Int. J. Therm. Sci.*, 44:1013–1023, 2005.
- [19] E. Larsen, J. Morel, and J. McGhee. Asymptotic derivation of the multigroup P_1 and simplified P_N equations with anisotropic scattering. *Nucl. Sci. Eng.*, 123:328–367, 1996.
- [20] E. Larsen, G. Thömmes, A. Klar, M. Seaid, and T. Götz. Simplified P_N approximations to the equations of radiative heat transfer and applications. *J. Comp. Phys.*, 183:652–675, 2002.
- [21] D. Mihalas and B.S. Mihalas. *Foundations of Radiation Hydrodynamics*. Oxford University Press, New York, 1983.
- [22] M.F. Modest. *Radiative Heat Transfer*. McGraw-Hill, 1993.
- [23] M. Seaid, M Frank, A. Klar, R. Pinnau, and G. Thömmes. Efficient numerical methods for radiation in gas turbines. *J. Comp. Applied Math.*, 170:217–239, 2004.
- [24] M. Seaid and A. Klar. Efficient preconditioning of linear systems arising from the discretization of radiative transfer equation. *Lect. Notes. Comp. Sci.*, 35:211–236, 2003.

- [25] P. Solin, K. Segeth, and I. Dolezel. *Higher-Order Finite Element Methods*. Chapman and Hall, 3–159, 2004.
- [26] G. Thömmes, R. Pinnau, M. Seaid, T. Götz, and A. Klar. Numerical methods and optimal control for glass cooling processes. *Transp. Theory Stat. Phys.*, 31:513–529, 2002.
- [27] R. Viskanta and E.E. Anderson. Heat transfer in semitransparent solids. *Advances in Heat Transfer*, 11:317–441, 1975.